April 7th, 2020

Editors
Tectonics

Dear Editors,

We are pleased to submit the enclosed manuscript entitled "*Late Quaternary uniform deformation in the foreland of the North Qilian Shan, NE Tibet*", which we wish to be considered for publication in *Tectonics*. We believe that this research provides some new insights into the deformation in the foreland of North Qilian Shan as follows, which would make the paper an appropriate candidate for publication in *Tectonics*.

(1) The activity of the Minle Fault has rarely been revealed, although the fault is an important part of the North Qilian Frontal Thrust. Our results show that the Minle Fault slips at a nearly constant rate in different periods of the late Pleistocene, and has been active since the Holocene, indicating that the deformation has spread into the Zhangye Basin. Active tectonics and GPS data indicate the uniform deformation in the Zhangye Basin but different shortening rates in the eastern and western basin. We attempted to explain the differences by different wedge structures. Previous studies concerning the deformation of the North Qilian Shan mostly focused on its interior or marginal area. However, the deformation of the foreland basins, the Hexi Corridor, are lacking concerns. The Zhangye Basin has complex tectonics, and its differential mode is representative in the deformation of the Hexi Corridor.

(2) We propose that the deformation of the tectonics in the north Qilian Shan, including the Minle Fault, is uniform in 10^4-year timescale and is inferred to be consistent with that in 10^6-year timescale. It implies that the Tibetan Plateau grows at a steady rate in 10^6-year timescale.

We confirm that this manuscript has not been published elsewhere and is not under consideration by any other journal. All of the authors agree with submission to *Tectonics*. Our results on deformation in the foreland of the North Qilian Shan should be of interest to researchers concerning with the usage of deformed river terrace in documenting active tectonics and researchers concerning with the late Quaternary deformation of the foreland of the North Qilian Shan in the northeastern Tibetan Plateau.

Thank you for your consideration of our manuscript. We look forward to your reply.

Sincerely yours,
Qingri Liu
Youli Li
Jianguo Xiong
Huiping Zhang
Weipeng Ge
Xudong Zhao
Xiu Hu
Yuezhi Zhong
Weilin Xin

Late Quaternary uniform deformation in the foreland of the North Qilian Shan, NE Tibet

Qingri Liu [1], Youli Li [1], Jianguo Xiong [2], Huiping Zhang [2], Weipeng Ge [3], Xudong Zhao [2], Xiu Hu [1], Yuezhi Zhong [4], Weilin Xin [1]

[1] *Key Laboratory of Earth Surface Processes of Ministry of Education, Peking University, Beijing 100871, China*

[2] *State Key Laboratory of Earthquake Dynamics, Institute of Geology, China Earthquake Administration, Beijing 100029, China*

[3] *Lanzhou Institute of Seismology, China Earthquake Administration, Lanzhou, China*

[4] *Department of Earth Sciences, ETH Zurich, Sonneggstrasse 5, 8092 Zurich, Switzerland*

Corresponding author: Qingri Liu (liuqingri@pku.edu.cn)

Key Points:

- The steady shortening rate of the Minle Fault since the late Pleistocene has been estimated to be 0.95±0.30 mm/a.
- Spatial difference in shortening rates was possibly caused by different wedge structures across the eastern and western Zhangye Basin.
- Deformation in the north Qilian Shan has been uniform in different timescales since the late Miocene.

Abstract

The Qilian Shan, in the northeastern Tibetan Plateau, has been continuously extending to the foreland since the late Cenozoic, resulting in the deformation of the Hexi Corridor Basins. Five terraces of the Hongshui River are faulted in the southern Zhangye Basin, a sub-basin of the Hexi Corridor, documenting the tectonic history of the Minle Fault since the late Quaternary. In this study, a high precision digital elevation model (DEM) generated by the unmanned aerial vehicle (UAV) photogrammetry is used to obtain the cumulative vertical offset of each terrace, and the abandonment ages of terraces are dated by AMS ^{14}C dating. The results show that the Minle Fault has been active since the Holocene, and produced an almost constant shortening rate of 0.95 ± 0.30 mm/a since 42.3 ± 0.5 ka, indicating that the deformation has spread into the Zhangye Basin. Active tectonics and GPS data indicate the uniform deformation in the Zhangye Basin but different shortening rates in the eastern and western basin. The differential allocation of deformation could have been caused by different wedge structures. Deformation of the North Qilian Fold-Thrust System (NQFTS) has been uniform since the late Quaternary and may be consistent with that in 10^6-year timescale, although further studies are needed.

Plain Language Summary

The foreland of the north Qilian Shan is the northeastern frontal zone of the Tibetan Plateau. Activities of the foreland reflect the growth rhythm of the plateau. Active tectonics and GPS data reveal steady shortening rates of the Zhangye Basin in 10^4 and 10 year-timescale, respectively. Deformation of the North Qilian Fold-Thrust System, including the Minle Fault, is uniform in 10^4 year-timescale. Inferred from the results of thermochronology, sedimentary stratigraphy, and

topography of the mountains, tectonics of the foreland exhibit uniform deformation in 10^6-year timescale. Our results imply that the overall growth rate of the northeastern Tibetan Plateau may be steady in 10^6 and 10^4 year-timescale.

1. Introduction

Since the Cenozoic, the India-Eurasia collision has resulted in the rapid uplift of the Tibetan Plateau with an average altitude of 4500 m. The plateau is still growing northward and eastward up to now, acting as a natural laboratory for understanding the mechanism of plate movement and tectonic activities, and its initial and peripheral blocks have been one of the most active regions around the world (Figure 1a; Meyer et al., 1998; Tapponnier et al., 2001; Searle et al., 2011). As the most leading edge of propagation, the northeast Tibet is a growing plateau with active tectonic movement and large earthquakes (Wang et al., 2014; Li et al., 2018; Zheng et al., 2019). A large number of studies have shown that the rapid uplift and tectonic deformation in the northeast Tibet initiated around 15 Ma (Zhu & Helmberger, 1996; de la Torre et al., 2007; Elliott et al., 2010; Wang et al., 2018), and the growth pattern may be progressively northward expansion (Li et al., 2013; Zheng et al., 2017a). The Qilian Shan, located in the northeast Tibet, with an area of ~250000 km^2 and an average altitude of ~4 km, is one of the key areas to study the latest expansion (Figure 1a). With ~50 km crustal shortening since the Miocene (Tapponnier et al., 2001; Meyer et al., 1998; Zheng et al., 2010; Zuza et al., 2016), the Qilian thrust belt can be considered as an ideal, active and small-scale model of the Tibetan Plateau, and its neotectonic features are of referential importance for comprehending the plateau growth (Zhang et al., 2017).

105 The Hexi Corridor, the foreland basins of the Qilian organic belt, has undergone continuous
106 deformation since the Neogene (Meyer et al., 1998; Tapponnier et al., 2001; Chen, 2003;
107 Champagnac et al., 2010). The south margins of the basins are controlled by a series of NW-SE-
108 strike folds and faults, including the Hanxia-Dahuanggou Fault (HDF), Laojunmiao Anticline,
109 Yumen Fault (YMF), Fodongmiao-Hongyazi Fault (FHF), North Yumu Shan Fault (NYSF),
110 Yumu Shan Anticline, East Yumu Shan Fault (EYSF), Minle Fault, Yonggu Anticline, Minle-
111 Damaying Fault (MDF), Huangcheng-Taerzhaung Fault (HTF), and Nanying Anticline. They are
112 collectively known as North Qilian Fold-Thrust System (NQFTS), clearly defining the boundary
113 of the Qilian Shan and the Hexi Corridor. In recent years, many studies have been conducted on
114 the NQFTS. The HDF is considered to be inactive during the late Quaternary (Chen, 2003; Liu et
115 al., 2017), while the other faults of the NQFTS have been active since the Holocene except the
116 Minle Fault (Li et al., 1997; Chen, 2003; Li et al., 2016; Xiong et al., 2017; Chen et al., 2017;
117 Yang et al., 2018a). The Minle fault may have initiated in the late Neogene inferred from the
118 affected strata, and it was still active in the Pleistocene (Institute of Geology and Lanzhou
119 Institute of Seismology (IGLS), 1993). As the studies on the Minle Fault are rare, the kinematics
120 of the fault need to be studied in detail. Continual deformation has propagated to the Hei Shan-
121 Longshou Shan in the north, forming another series of strike faults, which control the north
122 margin of the Hexi Corridor (Figure 1a; Zheng et al., 2013a, 2013b; Zhang et al., 2016). The
123 Hexi Corridor has played an important role in accommodating the crustal deformation of the
124 plateau; thus, its amount of shortening cannot be ignored (Yang et al., 2018b). The regional
125 shortening can be derived by interpreting the seismic reflection profile and then restoring the
126 balanced profile according to the surface geology and regional tectonic history (Dahlstrom, 1969;

127 Zuza et al.,2016). But the seismic data are limited in the Hexi Corridor. However, the shortening
128 rate can be estimated by adding the shortening rates of the known structures in the basins. In this
129 way, the estimated shortening rate of the Jiuxi Basin (~2.2 mm/a, Liu et al., 2017) is slightly
130 higher than that of the Jiudong Basin (~1.3~2.2 mm/a, Yang et al., 2018b), implying that the
131 shortening rate of the Hexi Corridor is not consistent. The Zhangye Basin has more complex
132 active tectonics than the Jiudong Basin and its shortening rate remains less well constrained. In
133 the west Zhangye Basin, the Yumu Shan uplift is extruded, while faults and folds exist within the
134 east basin. This differential mode is helpful for understanding the spatial variation of deformation
135 in the Hexi Corridor.
136
137 The spatiotemporal uniformity of the deformation on the NQFTS is still in controversy. The
138 shortening rate of the FHF at the mouth of the Hongshuiba River is considered to be 1.0~1.4
139 mm/a (Yang et al., 2018a) or 2.0±0.3 mm/a (Hetzel et al., 2019). However, all the other studies
140 on the whole fault show that the shortening rates are ~1 mm/a (Yang et al., 2018b; Liu et al.,
141 2019a). The shortening rates of the YMF (Liu et al., 2017) and the MDF (Xiong et al., 2017) are
142 both close to 1 mm/a. It seems that the east and west portions of the NQFTS may produce
143 shortening rates at the same order of magnitude (Yang et al., 2018b; Cao et al., 2019). In
144 addition, the shortening rate of the NQFTS in 10^4-year timescale has increased, compared with
145 that in 10^6-year timescale (Champagnac et al., 2010), but other researchers believed that the
146 NQFTS may have slipped at a nearly constant rate in different timescales (Zhao et al., 2017;
147 Hetzel et al., 2019).
148

149 The Minle Fault is located in the central part of the NQFTS, and has faulted a series of fluvial
150 terraces of the Hongshui River. In this study, a DEM derived from a UAV was applied in
151 determining the accurate vertical offset of the Minle Fault, and AMS ^{14}C dating were used to date
152 the abandonment ages of the terraces. Our aims are to (1) estimate the shortening rate of the
153 Minle Fault, (2) understand the deformation across the Zhangye Basin and northeastward
154 expansion of the NQFTS, and further to (3) discuss the uniformity of deformation on the NQFTS
155 including the Minle Fault.

156 **2. Geological setting**

157 The north Qilian fold belt is a complex anticline belt, the axis of which is mainly composed of
158 Cambrian and Ordovician strata, while the flanks are mostly Ordovician and Silurian strata
159 (IGLS, 1993). The Hexi Corridor has been a strongly-sinking region since the Tertiary,
160 surrounded by the Qilian Shan in the south and Hei Shan-Longshou Shan in the north. The Hexi
161 Corridor basins are partitioned into 4 sub-basins, namely, the Jiuxi Basin, Jiudong Basin,
162 Zhangye Basin, and Wuwei Basin, separated by the Wenshu Shan, Yumu Shan, and Dahuang
163 Shan, from west to east, respectively (IGLS, 1993). The base of these basins mainly consists of
164 early Paleozoic strata, covered by highly thick Mesozoic and Cenozoic sediments (IGLS, 1993).
165 With the Dahuang Shan and Yumu Shan respectively constraining its eastern and western
166 boundaries, the Zhangye Basin has received about 1000 m-thick Neogene and Quaternary
167 deposits (Figure 1b; IGLS, 1993).

168

169 The south margin of the Zhangye Basin is controlled by the MDF, the Minle Fault, the EYSF and
170 the NYSF, and its north margin is defined by the South Longshou Shan Fault (SLSF) and the

South Heli Shan Fault (SHSF). The MDF extends to NWW over a length of 200 km and dipping SW at varying angles from 60° to 70°. It is an obvious thrust fault, being active as early as the late Tertiary (IGLS, 1993). As shown in recent studies, the MDF still has been very active since the Holocene, with vertical slip rates up to 1 mm/a in the east and west (Zhong, 2017; Xiong et al., 2017). Extending along the eastern edge of the Yumu Shan over a length of 110 km and dipping SW at angles of 40°~60°, the EYSF consists of two secondary faults with Matisi as the segmentation point. Different segments of the fault initiated from the end of Miocene to the end of Pleistocene (IGLS, 1993). Since the late Pleistocene, the EYSF has slipped at a vertical rate of 1 mm/a near the mouth of the Hei River (Qi, 2017; Ren et al., 2019; Cao et al., 2019). The NYSF extends to NWW or NW on the alluvial fans at the north edge of the Yumu Shan, dipping 40°~80° to the SW over a distance of 60 km (IGLS, 1993). The late Pleistocene rate of the vertical slip on the fault has been estimated to be ~0.7 mm/a (Palumbo et al., 2009; Chen et al., 2017). The SLSF and SHSF define the boundary of the Alxa block and Hexi Corridor. The SLLSF, extending NWW from Hexipu to Gaotai with a total length of 270 km and dipping SW at angles of 60°~70°, has been still active in the Quaternary (IGLS, 1993). The SHSF is separated into three sections from Xiaojiazhuang to Hongtugou, extending to 50° N~60° W over a length of 65 km with dip angles varying from 40° to 80° along the strike (Zheng et al., 2013a). Its average vertical slip rate has been estimated as 0.1~0.3 mm/a since the late Pleistocene (Zheng et al., 2013a).

Located in the south of the Dahuang Shan, the Minle-Yongchang Blind Fault and the Yonggu Anticline develop in the Zhangye Basin. They have been active since the late Pleistocene, and

193 have caused the Ms 4.8 earthquake in 1978, Ms 5.8 and 6.1 earthquakes in 2003, and Ms 5.3
194 earthquake in 2007 (Figure 1b; Zheng et al., 2005; Zou et al., 2017). The Yonggu Anticline slips
195 at a shortening rate of 1.50±0.06 mm/a over the past ~10 ka, absorbing the main shortening of
196 the basin (Zhong, 2017). The neotectonics of the Zhangye Basin has mainly formed (1) the
197 differential uplift regions since the Tertiary, such as the Yumu Shan and the Dahuang Shan, (2)
198 the differential uplift regions since the Quaternary represented by the Yonggu Anticline, and (3)
199 the slight uplift region represented by piedmont facies around the Yumu Shan and the Dahuang
200 Shan (Wang & Xu, 1990; IGLS, 1993).
201
202 The Minle Fault, 15 km long, is connected to the MDF in the south and the EYSF in the
203 northwest (Figure 1b). It extends N-S-strike in the south section and NW-strike in the north
204 section. Obvious thrusting can be observed in the latter section (Figures 2b and 5). The fluvial
205 terraces of the Hongshui River were continuously offset by the Minle Fault. The Pliocene red
206 sandstones, as the base underlying the Quaternary fluvial deposits, are exposed in the hanging
207 wall of the fault (Figures 2c and 3). Responding to the activities of the Minle Fault, the
208 Hongshui River and its tributaries turn to NNW out of the Qilian Shan (Figure 2b; IGLS, 1993).

209 **3. Method**

210 **3.1. Terrace Mapping**

211 We divided the terraces of the Hongshui River into seven levels, and mapped them on the Google
212 satellite imagery (Figure 2a). The geomorphic features of the terraces were obtained by the
213 following 5 steps: (1) We recognized the shape of the terraces and drew them on the Google map,

(2) summarized the sedimentary characteristics of each terrace, including color, thickness, grain size, roundness, and components, and stratified the sediments, (3) measured the height of each terrace relative to the riverbed by a TruPulse 200X laser range finder, (4) graded the terraces on the map according to the elevation and the sedimentary structure, and finally (5) drew the terrace-to-river cross sections (Figure 3).

The terrace T_7 only appears on the west bank of the Hongshui River, a part of the hanging wall, and only the erosion remains are scattered in the area. The terraces T_6, T_5, T_3, and T_2 are widely distributed on the east bank with continuous and flat surfaces, whereas partly developed on the west bank with narrow and broken surfaces due to erosion. On the east bank, the terraces T_5, T_3, and T_2 are disrupted by the Minle Fault, enabling us to trace the fault. The terrace T_4 is restrictedly reserved on the banks near the Shangwan village, and the terrace T_1 scatters on both banks with limited areas (Figure 2a). In the hanging wall, the Pliocene red sandstones, the base of the terraces, are exposed on both banks with continuous and flat surfaces, underlying the fluvial sediments of 1-8 m (T_1-T_5), and 20-60 m (T_6-T_7) and eolian loess of 1-20 m. After investigation, the terraces T_1-T_4 in the hanging wall are all confirmed to be strath terraces, while the terrace T_5 and T_7 are aggradational terraces (Figure 3). The fluvial sediments on the terraces are mainly composed of round or sub-round gravels, some of which are boulders of decimeter size. The lithology of these gravels is mainly conglomerate, sandstone, limestone, metasandstone, and slate.

The terraces T_1, T_2, T_3, T_4, and T_5 of the Hongshui River are offset by the Minle Fault along its

NW strike, forming a series of NE-facing scarps as ideal media for studying the kinematics of the fault (Figure 2b). The average dip angle on a natural outcrop of the terrace T_1 is 31°±7°, which will be used as the thrust angle of this fault (Figure 2c).

3.2. Sampling and AMS ^{14}C Dating

Eight charcoal samples were collected from the overlying sand layers or within the gravel layers of the T_1, T_2, and T_5. No suitable material for dating was found in the fluvial deposits of the terraces T_3 and T_4. Thus, their abandonment ages remain unconstrained. To ensure the accuracy of the age, we collected three samples on the terrace T_1. Samples MLF97, MLF123, and MLF125 were taken from the fluvial sand layer overlying the gravel layer (Figures 4a and 4b). Another three samples were collected on the terrace T_2. Among them, samples MLF79 and MLF113 were collected from the overlying sand layer, while sample MLF25 was from the sand layer within the gravel layer (Figures 4c-4e). We obtained two samples at the same site from the terrace T_5, including sample MLF38 from the overlying sand layer and sample MLF39 from the gravel layer (Figure 4f).

All collected charcoal samples were sent to the Beta laboratory for AMS ^{14}C age test to determine the abandonment age of the terraces. The laboratory treated the samples following the standard experimental procedure (Vries & Barendsen, 1954). All the samples were pretreated with an acid-alkali-acid sequence to remove contaminants, and then they were converted into graphite samples, which were used for the radiometric C determination by AMS.

3.3. Unmanned aerial vehicle Photogrammetry

Using a UAV equipped with a camera to obtain aerial images has progressively become an important method in geomorphology research. The image with GPS system can generate DEMs with the ground resolution up to centimeter level. In this study, the UAV, the Dajiang phantom 4 Pro, was equipped with a 1-inch outsole Sony Exmor R CMOS sensor of 20 megapixel, and with a satellite positioning module (GPS/GLONASS). According to the principle of "uniform-distributed and non-collinear points", nineteen control points and two check points were set in the planned area before the flight. We used the Trimble GEO7X handheld GPS to determine the geographic coordinates of these points with the precisions of less than 5 cm (Figure 5c). Based on the topography of the study area, the aerial photo height was set to 230 m. After arraying the photo, adding control points, creating the dense point clouds, and building the grids in the software of Agisoft Photoscan 1.4, an orthophoto image with an area of 2.09 km^2 and a ground resolution of 5.91 cm/pix was acquired (Figure 5a), and a DEM with horizontal and vertical accuracy of 0.6 m and 0.2 m, respectively, was finally exported (Figure 5d).

The terraces T_1, T_2, T_3, T_4, and T_5 were recognized on the DEM, and three topographic profiles across the fault were extracted from each terrace except the terrace T_1 (Figures 5b and 5d). Assuming that the erosion and deposition flux are zero, the height of the scarp on the profile can represent the cumulative vertical offset of the fault since the terrace was abandoned. We took the mean height of the scarps on the three profiles as the vertical offset of each terrace. Because the terrace T_1 has been eroded, no topographic profiles were extracted from it.

4. Results

4.1. Determination of the abandonment age

The three samples of the terrace T_1 collected from the overlying sand layer can represent the abandonment age. The age differences between samples MLF123 and MLF125 from the same site is about 0.1 ka, while sample MLF97 from another site is ~0.4 ka older than the former two. The ages of the three samples approach each other, implying that they are reliable. Thus, we take the average age of 9310±87 cal a BP as the abandonment age of the terrace T_1 (Table 1). Among the three samples of the terrace T_2, samples MLF79 and MLF113 are from the overlying sand layer, while sample MLF25 is from the sand within the gravel layer. Their ages all fall into the late MIS 2 stage, although they are inverted to some extent. The average age of 17513±185 cal a BP is calculated to represent the abandonment age of the terrace T_2 (Table 1). The two samples of the terrace T_5 are from the same exposure. Sample MLF38 from the overlying sand layer can represent the abandonment age, while sample MLF39 from the sand within the gravel layer can represent the maximum age for abandonment. Sample MLF39 is about 4 ka older than MLF38, consistent with the sedimentary law that the lower layers are older than the upper layers in a normal sedimentary sequence. Therefore, the age of sample MLF38 is taken as the abandonment age of the terrace T_5 (Table 1). The ages of the three terraces exhibit a good sequence, and the terraces with the ages of ~40 ka (Chen, 2003; Liu et al., 2017; Yang et al., 2018a; Ren et al., 2019), ~18 ka (Palumbo et al., 2009; Liu et al., 2017; Hetzel et al., 2019), and ~9 ka (Chen et al., 2017; Zhong, 2017; Liu et al., 2019a) are widely developed at the northern foot of the Qilian Shan, which show the robust chronology of this study.

4.2. Vertical offset of the Minle Fault

The faulted terrace T_1 indicates that the Minle Fault is still active in the Holocene (Figures 2c and 5b). The cumulative vertical offsets recorded by the other terraces decrease sequentially. The vertical offsets of the terraces T_5, T_4, T_3, and T_2 are 23.0±0.6 m, 16.4±0.2 m, 12.5±0.5 m, and 8.6±0.2 m, respectively. Therefore, the vertical offset of the terraces T_5 is a cumulation on account of multiple-stage activities (Figure 6).

4.3. Estimate of the shortening rate on the Minle Fault

Combining the abandonment ages of the faulted terraces and the vertical offsets recorded by each terrace, the slip rates of the fault can be calculated. The uncertainty is estimated based on the uncertainty of the age and the vertical offset. First, the vertical offset is divided by the abandonment age to get the vertical slip rate (vertical component of the fault slip rate) in different periods. As a result, the vertical slip rate of the Minle Fault is 0.54±0.02 mm/a since the abandonment of the terrace T_5 (42.3±0.5 ka), which approaches the rate of 0.49±0.01 mm/a since the abandonment of the terrace T_2 (16.9±0.2 ka). The linear regression analysis of the vertical slip rates of the two terraces through the original point shows that the correlation coefficient is almost equal to 1, indicating that the Minle Fault has a long-term steady slip rate (Figure 7). Finally, the shortening rate (horizontal component of the slip rate) of 0.95±0.30 mm/a is calculated based on trigonometrical function and the thrust angle of 31°±7°. In fact, the terraces in the hanging wall of the fault have suffered erosion while the terraces in the foot wall have accepted the deposition after being faulted, which means the measured fault scarp may be smaller than the real offset. In addition, the age of the charcoal from the sand overlying the gravel layer cannot fully represent the cutting age of the river, but a little earlier than the

abandonment age. Therefore, the slip rate of the Minle Fault is likely to be slightly underestimated.

5. Discussion

5.1. Differential deformation of the Zhangye Basin

The slip rates of the Minle Fault since 42.3±0.5 ka and 16.9±0.2 ka are close to each other (Figure 7). Similarly, the differences among the vertical slip rates on the MDF in different periods since 12.7±1.4 ka are less than 0.05 mm/a (Figure 8; Xiong et al., 2017). Furthermore, the vertical slip rates of the NYSF in the three periods since 113.4±4.9 ka are all about 0.6 mm/a, and that of the EYSF since 47.0±3.4 ka and 19.69±1.32 ka are 1.25 mm/a and 1 mm/a, respectively (Figure 8; Qi, 2017). Overall, the rates of deformation in the south margin of the Zhangye Basin have been almost constant since the late Pleistocene. By summarizing or calculating the shortening rates of the faults, as shown in Table 2, the shortening rate of the Minle Fault (0.95±0.30 mm/a) is close to that of the MDF (1.15±0.75 mm/a), but higher than that of the NYSF (0.52±0.33 mm/a) and the EYSF (0.6±0.3 mm/a). Recently, the NYSF has been observed to control the deformation of the anticline in its hanging wall although the shortening rate on the fault itself is low (Hu et al., 2019). The total shortening rate of the fault-fold system reaches 1.8±0.4 mm/a, most part of which was absorbed by the anticline (Hu et al., 2019). Likewise, the deformation is possible to be absorbed by the fault-related fold in the east Yumu Shan. Among the faults in the north margin of the Zhangye Basin, the SLSF has caused a 20-meter scarp since the late Pleistocene (IGLS, 1993), but the slip rate has not been constrained. Inferred from the similar tectonic settings and geometries of the Longshou Shan

and the Heli Shan, the shortening rate of the SLSF is assumed to be close to that of the SHSF (~0.4 mm/a; Table 2; Figure 8; Zheng et al., 2013a).

Different shortening rates are observed across the eastern and western Zhangye Basin. In the eastern basin, the deformation is mainly allocated to the Minle Fault or MDF, the Yonggu Anticline (with a shortening rate of 1.50±0.06 mm/a; Zhong, 2017), and the SLSF. While in the western basin, the fault-fold system in the north Yumu Shan (Hu et al., 2019) and the SHSF (Zheng et al., 2013a) are responsible for the shortening. The shortening rates of the eastern and western Zhangye Basin are 2.85±0.36 mm/a and 2.1±0.6 mm/a, respectively, derived from the active tectonics. They are consistent with shortening rates of 2.92±1.01 mm/a and 1.93±0.96 mm/a derived from GPS data (Zheng et al., 2017b). In addition, the southern Zhangye Basin absorbs ~84% and ~76% of the deformation across the whole basin in the eastern and western basin, respectively (Figure 9). Thus, the NQFTS is the dominant tectonics in the Hexi Corridor, although thrusts exist in both margins of the basins.

As mentioned above, results in 10^4-year timescale and GPS observation velocities in 10-year timescale both show that deformation rates in the south margin of the Zhangye Basin are steady, but differences exist between the eastern and western basin. The differential allocation of deformation is inferred to be caused by different accretionary wedge structures in the upper crust. Active folds exist in the hanging wall of the NYSF, but no active fold has been found in the hanging wall of the MDF (Zhong, 2017; Lei et al., 2020), while the Yonggu Anticline develops within the basin in the north of the MDF. Under continuous compression, the wedge grows and

363 the materials within are deformed until the critical taper is attained, which depends on the
364 strength of the base relative to the internal strength of the wedge (Davis et al., 1983). After that, it
365 slides stably, continuing to grow self-similarly as a constant taper when encountering other
366 materials at the toe (Davis et al., 1893). Thermochronology (Zheng et al., 2010) and sedimentary
367 stratigraphy (Bovet et al., 2009; Wang et al., 2016) reveal that the north frontal faults of the west
368 Qilian initiated at ~10 Ma. Considering that the overall uplift of the east and west Qilian has
369 resulted in the similar topography and deformation of the involved strata, we infer that the north
370 frontal faults in the east Qilian, represented by the MDF, initiate at ~10 Ma. The NYSF began to
371 be active at ~4 Ma (Palumbo et al., 2009; Hu et al., 2019), but the Yonggu Anticline seems to be
372 younger, inferred from topography and actual research (Zhong, 2017). Based on the above
373 analysis, the wedge taper of the NYSF is inferred to float around the critical taper due to the
374 erosion, thus the wedge is deformed internally. However, the upper crustal wedge of the MDF
375 may have exceeded the critical taper due to its long-history activity. As a result, instead of
376 causing the fold in its hanging wall to be deformed, the MDF slips and accretes forward to the
377 Yonggu Anticline. Due to the younger formation age, the Yonggu Anticline is far from reaching
378 the critical taper, so the fault slip is not significant, mainly manifested as internal fold
379 deformation.

380 **5.2. Uniform deformation in the north margin of the Qilian Shan**

381 As discussed in the previous section, the faults in the south margin of the Zhangye Basin,
382 including the Minle Fault, have produced nearly constant slip rates since the late Pleistocene. In
383 addition, the other faults or folds of the NQFTS, such as the YMF (Liu et al., 2017), FHF (Yang
384 et al., 2018a), HTF (Chen, 2003), and Nanying Anticline (Hu et al., 2015) also seem to exhibit

steady-rate activities in 10^4-year timescale (Figure 8; Table 2). If the surveying and the chronology of these studies are reliable, the crustal deformation in 10^4-year timescale in the north margin of the Qilian Shan is relatively uniform. It indicates that the NQFTS has been the most active boundary in the northeast front of the Tibetan Plateau, and that the Qilian Shan is gradually growing into a plateau.

The shortening rate revealed by thermochronology since ~10 Ma (Zheng et al., 2010) is consistent with the shortening rate derived from the active tectonics since the late Pleistocene (Yang et al., 2018a, 2018b; Liu et al., 2019a), indicating that the slip rate of the FHF may be steady in the long term. The estimated shortening rate of 0.72 mm/a of the Laojunmiao Anticline since ~5 Ma (Zhao et al., 2017) is within the range of that of 0~2.2±0.5 mm/a in 10^4-year timescale (Hetzel et al., 2006). Based on the matching of the present topography with the slip rate of the relevant fault, the Yumu Shan (Palumbo et al., 2009), Heli Shan (Zheng et al., 2013a), and Jintanan Shan (Zheng et al., 2013b) are considered to have grown at a steady rate since ~4 Ma, ~2 Ma, and ~1.5 Ma, respectively. It seems that the faults in the north margin of the west Qilian Shan and even the mountains in the north of the Hexi Corridor exhibit uniform deformation in 10^6-year timescale. Although the east Qilian lacks the tectonic results in 10^6-year timescale, its topography, stratigraphy, and slip rate of the northern boundary faults are similar to those of the west Qilian (Figure 8). Moreover, the whole north Qilian is considered to be the result of rapid uplift since 10 Ma (Zheng et al., 2010). Thus, the deformation of the east Qilian is inferred to be also uniform in 10^6-year timescale, although more data are needed.

6. Conclusion

Five terraces of the Hongshui River in the south of the Zhangye Basin were faulted by the Minle Fault, documenting the tectonic history of the fault since the late Pleistocene. A DEM generated by the UAV photogrammetry is used to obtain the cumulative vertical offset of each terrace, and the abandonment ages of terraces are dated by AMS ^{14}C dating. The results show that the Minle Fault has been active since the Holocene, and that it has shortened steadily at a rate of 0.95± 0.30 mm/a since the late Pleistocene, indicating that the deformation has spread into the Zhangye Basin. Active tectonics and GPS data indicate the uniform deformation in the Zhangye Basin but different shortening rates in the eastern and western basin. The differential allocation of deformation could be caused by different wedge structures. Deformation of the NQFTS has been almost uniform since the late Quaternary and may be consistent with that in 10^6-year timescale, although further studies are needed.

Acknowledgement

The error data of the control points and check points (in Figure 5c), the high-resolution DEM data (in Figure 5d), and the data of the topographic profiles across the Minle Fault (in Figure 6) can be downloaded from https://doi.org/10.4121/uuid:d5e16253-ca8a-4cf2-aa33-52f3afcc61d4 (The DOI may have not been activated yet, because the dataset is waiting to be reviewed by the repository of 4TU. We temporarily upload a copy of our data as Supporting Information for review purposes, but the DEM data with a large size of ~400 MB cannot be uploaded as Supporting Information). GPS observation velocity across the Zhangye Basin in the direction of N45°E (in Figure 9) can be obtained in the Supporting Information (Table S1) and the related

reference. This research was jointly financed by the Fundamental Research Funds in the institute of Geology, China Earthquake Administration (Grant IGCEA1915), the Second Tibetan Plateau Scientific Expedition and Research Program (STEP, Grant No. 2019QZKK0704), the National Natural Science Foundation of China (Grants 41702219, 41571001, and 41872204), and the Foundation of the State Key Laboratory of Earthquake Dynamics (LED2017A04). Professor Gang Rao is appreciated for his very constructive comments on the manuscript.

References

Bovet, P. M., Ritts, B. D., Gehrels, G., Abbink, A. O., Darby, B., & Hourigan, J. (2009). Evidence of Miocene crustal shortening in the north Qilian Shan from Cenozoic stratigraphy of the western Hexi Corridor, Gansu Province, China. *American Journal of Science*, *309*(4), 290-329.

Cao, X., Hu, X., Pan, B., Zhang, J., Wang, W., Mao, J., & Liu, X. (2019). A fluvial record of fault-propagation folding along the northern Qilian Shan front, NE Tibetan Plateau. *Tectonophysics*, *755*, 35-46.

Champagnac, J. D., Yuan, D. Y., Ge, W. P., Molnar, P., & Zheng, W. J. (2010). Slip rate at the north‐eastern front of the Qilian Shan, China. *Terra Nova*, *22*(3), 180-187.

Chen, G., Zheng, W., Wang, X., Zhang, P., Xiong, J., Yu, J., Liu, X., Bi, H., Liu, J., & Ai, M. (2017). Present kinematics characteristics of the northern Yumushan active fault and its response to the northeastward growth of the Tibetan Plateau. *Seismology and Geology, 39*(5), 871-888. (in Chinese with English abstract).

Chen, W. (2003). Principal features of tectonic deformation and their generation mechanism in the Hexi Corridor and its adjacent regions since late Quaternary. PhD thesis of Institute of

449 Geology, China Seismological Bureau, Beijing, China, pp. 32-55. (in Chinese with English
450 abstract).
451 Dahlstrom, C. D. A. (1969). Balanced cross sections. *Canadian Journal of Earth Sciences*, *6*(4),
452 743-757.
453 Davis, D., Suppe, J., & Dahlen, F. A. (1983). Mechanics of fold-and-thrust belts and accretionary
454 wedges. *Journal of Geophysical Research: Solid Earth*, *88*(B2), 1153-1172.
455 De la Torre, T. L., Monsalve, G., Sheehan, A. F., Sapkota, S., & Wu, F. (2007). Earthquake
456 processes of the Himalayan collision zone in eastern Nepal and the southern Tibetan Plateau.
457 *Geophysical Journal International*, *171*(2), 718-738.
458 Elliott, J. R., Walters, R. J., England, P. C., Jackson, J. A., Li, Z., & Parsons, B. (2010). Extension
459 on the Tibetan plateau: recent normal faulting measured by InSAR and body wave
460 seismology. *Geophysical Journal International*, *183*(2), 503-535.
461 Hetzel, R., Hampel, A., Gebbeken, P., Xu, Q., & Gold, R. D. (2019). A constant slip rate for the
462 western Qilian Shan frontal thrust during the last 200 ka consistent with GPS-derived and
463 geological shortening rates. *Earth and Planetary Science Letters*, *509*, 100-113.
464 Hu, X., Pan, B., Kirby, E., Gao, H., Hu, Z., Cao, B., ... & Zhang, G. (2015). Rates and kinematics
465 of active shortening along the eastern Qilian Shan, China, inferred from deformed fluvial
466 terraces. *Tectonics*, *34*(12), 2478-2493.
467 Hu, X., Wen, Z., Pan, B., Guo, L., & Cao, X. (2019). Constraints on deformation kinematics
468 across the Yumu Shan, NE Tibetan Plateau, based on fluvial terraces. *Global and Planetary*
469 *Change*, *182*, 103023.
470 Institute of Geology, State Seismology Bureau, and Lanzhou Institute of Seismology, State

Seismology Bureau. (1993). The Qilian Shan-Hexi Corridor Active Fault System (pp.76-115). Beijing: Seismological Press. (in Chinese).

Lei, J., Li, Y., Oskin, M. E., Wang, Y., Xiong, J., Xin, W., ... & Liu, F. (2020). Segmented Thrust Faulting: Example from the Northeastern Margin of the Tibetan Plateau. *Journal of Geophysical Research: Solid Earth*, e2019JB018634.

Li, A., Wang, X. X., Zhang, S. M., Chen, Z. D., Liu, R., Zhao, J. X., & Lu, Y. W. (2016). The slip rate and paleoearthquakes of the Yumen fault in the Northern Qilian Mountains Since the Late Pleistocene. *Seismol. Geol.*, *38*(4), 897-910. (in Chinese with English abstract).

Li, Q., Pan, B., Hu, X., Hu, Z., Li, F., & Yang, S. (2013). Apatite fission track constraints on the pattern of faulting in the north Qilian Mountain. *Journal of Earth Science*, *24*(4), 569-578.

Li, Y., Liu, M., Wang, Q., & Cui, D. (2018). Present-day crustal deformation and strain transfer in northeastern Tibetan Plateau. *Earth and Planetary Science Letters*, *487*, 179-189.

Li, Y., Yang, J., Li, B., & Tan, L. (1997). On the tectonic landform of the Yumu Mountain, Hexi corridor, Gansu province. *Journal of Geomechanics, 3*(4), 20-26. (in Chinese with English abstract).

Liu, X., Yuan, D., Zheng, W., Shao, Y., Liu, B., & Gao, X. (2019a). Holocene slip rate of the frontal thrust in the western Qilian Shan, NE Tibetan Plateau. *Geophysical Journal International*, *219*(2), 853-865.

Liu, X. W., Yuan, D. Y., & Su, Q. (2019b). Late Pleistocene slip rate on a blind thrust in the western Qilian Shan, NW China. *Geomorphology*, *345*, 106841.

Liu, X. W., Yuan, D. Y., & Su, Q. (2017). Late Pleistocene slip rate of the northern Qilian Shan frontal thrust, western Hexi Corridor, China. *Terra Nova*, *29*(4), 238-244.

493 Meyer, B., Tapponnier, P., Bourjot, L., Metivier, F., GauUAer, Y., Peltzer, G., ... & Zhitai, C.
494 (1998). Crustal thickening in Gansu-Qinghai, lithospheric mantle subduction, and oblique,
495 strike-slip controlled growth of the Tibet plateau. *Geophysical Journal International*, *135*(1),
496 1-47.
497 Qi, R. (2017). The characteristics of river terraces of Heihe and Liyuan River in Hexi Corridor
498 and the response of its neotectonic movement. Master's Degree thesis of China University of
499 Geosciences, Beijing, China, pp. 54-56. (in Chinese with English Abstract).
500 Palumbo, L., Hetzel, R., Tao, M., Li, X., & Guo, J. (2009). Deciphering the rate of mountain
501 growth during topographic presteady state: An example from the NE margin of the Tibetan
502 Plateau. *Tectonics*, *28*(4), 1-18.
503 Reimer, P. J., Bard, E., Bayliss, A., Beck, J. W., Blackwell, P. G., Ramsey, C. B., ... & Grootes, P.
504 M. (2013). IntCal13 and Marine13 radiocarbon age calibration curves 0–50,000 years cal BP.
505 *Radiocarbon*, *55*(4), 1869-1887.
506 Ren, J., Xu, X., Zhang, S., Ding, R., Liu, H., Liang, O., & Zhao, J. (2019). Late Quaternary slip
507 rates and Holocene paleoearthquakes of the eastern Yumu Shan fault, northeast Tibet:
508 Implications for kinematic mechanism and seismic hazard. *Journal of Asian Earth Sciences*,
509 *176*, 42-56.
510 Searle, M. P., Elliott, J. R., Phillips, R. J., & Chung, S. L. (2011). Crustal–lithospheric structure
511 and continental extrusion of Tibet. *Journal of the Geological Society*, *168*(3), 633-672.
512 Tapponnier, P., Zhiqin, X., Roger, F., Meyer, B., Arnaud, N., Wittlinger, G., & Jingsui, Y. (2001).
513 Oblique stepwise rise and growth of the Tibet Plateau. *Science*, *294*(5547), 1671-1677.
514 De Vries, H. L., & Barendsen, G. W. (1954). Measurements of age by the carbon-14 technique.

Nature, *174*(4442), 1138-1141.

Wang, C., Dai, J., Zhao, X., Li, Y., Graham, S. A., He, D., ... & Meng, J. (2014). Outward-growth of the Tibetan Plateau during the Cenozoic: A review. *Tectonophysics*, *621*, 1-43.

Wang, D., & Xu, X. (1990). Neotectonics and Seismicity of Minle Basin in Gansu province. *Gansu Geology, 11*, 24-35. (in Chinese with English abstract).

Wang, W., Zhang, P., Pang, J., Garzione, C., Zhang, H., Liu, C., ... & Yu, J. (2016). The Cenozoic growth of the Qilian Shan in the northeastern Tibetan Plateau: A sedimentary archive from the Jiuxi Basin. *Journal of Geophysical Research: Solid Earth*, *121*(4), 2235-2257.

Wang, Y., Zheng, D., Pang, J., Zhang, H., Wang, W., Yu, J., ... & Li, Y. (2018). Using slope-area and apatite fission track analysis to decipher the rock uplift pattern of the Yumu Shan: New insights into the growth of the NE Tibetan Plateau. *Geomorphology*, *308*, 118-128.

Xiong, J., Li, Y., Zhong, Y., Lu, H., Lei, J., Xin, W., ... & Zhang, P. (2017). Latest Pleistocene to Holocene thrusting recorded by a flight of strath terraces in the eastern Qilian Shan, NE Tibetan Plateau. *Tectonics*, *36*(12), 2973-2986.

Yang, H., Yang, X., Huang, X., Li, A., Huang, W., & Zhang, L. (2018a). New constraints on slip rates of the Fodongmiao-Hongyazi fault in the Northern Qilian Shan, NE Tibet, from the ^{10}Be exposure dating of offset terraces. *Journal of Asian Earth Sciences*, *151*, 131-147.

Yang, H., Yang, X., Zhang, H., Huang, X., Huang, W., & Zhang, N. (2018b). Active fold deformation and crustal shortening rates of the Qilian Shan Foreland Thrust Belt, NE Tibet, since the Late Pleistocene. *Tectonophysics*, *742*, 84-100.

Yuan, D. Y., Ge, W. P., Chen, Z. W., Li, C. Y., Wang, Z. C., Zhang, H. P., ... & Dayem, K. E. (2013). The growth of northeastern Tibet and its relevance to large-scale continental

geodynamics: A review of recent studies. *Tectonics, 32*(5), 1358-1370.

Zhang, H., Zhang, P., Prush, V., Zheng, D., Zheng, W., Wang, W., ... & Ren, Z. (2017). Tectonic geomorphology of the Qilian Shan in the northeastern Tibetan Plateau: Insights into the plateau formation processes. *Tectonophysics*, *706*, 103-115.

Zhang, N., Zheng, W. J., Liu, X. W., Wang, W. T., Li, X. N., He, W. G., ... & Shao, Y. X. (2016). Kinematics characteristics of Heishan fault in the western Hexi Corridor and its implications for regional tectonic transformation. *J. Earth Sci. Environ.*, *38*(2), 245-257. (in Chinese with English abstract).

Zhao, Z., Granger, D. E., Chen, Y., Shu, Q., Liu, G., Zhang, M., ... & Yan, Y. (2017). Cosmogenic nuclide burial dating of an alluvial conglomerate sequence: an example from the Hexi Corridor, NE Tibetan Plateau. *Quaternary Geochronology*, *39*, 68-78.

Zheng, D., Clark, M. K., Zhang, P., Zheng, W., & Farley, K. A. (2010). Erosion, fault initiation and topographic growth of the North Qilian Shan (northern Tibetan Plateau). *Geosphere*, *6*(6), 937-941.

Zheng, D., Wang, W., Wan, J., Yuan, D., Liu, C., Zheng, W., ... & Zhang, P. (2017a). Progressive northward growth of the northern Qilian Shan–Hexi Corridor (northeastern Tibet) during the Cenozoic. *Lithosphere*, *9*(3), 408-416.

Zheng, G., Wang, H., Wright, T. J., Lou, Y., Zhang, R., Zhang, W., ... & Wei, N. (2017b). Crustal deformation in the India‐Eurasia collision zone from 25 years of GPS measurements. *Journal of Geophysical Research: Solid Earth*, *122*(11), 9290-9312.

Zheng, W., He, W., Zhao, G. & Maima. (2005). Discussion on the causative structure and mechanism of the 2003 Minle-Shandan, Gansu, M6.1, 5.8 Earthquakes. *Journal of*

Seismological Research. 28(2), 133-140. (in Chinese with English Abstract).

Zheng, W. J., Zhang, P. Z., Ge, W. P., Molnar, P., Zhang, H. P., Yuan, D. Y., & Liu, J. H. (2013a). Late Quaternary slip rate of the South Heli Shan Fault (northern Hexi Corridor, NW China) and its implications for northeastward growth of the Tibetan Plateau. *Tectonics*, *32*(2), 271-293.

Zheng, W. J., Zhang, H. P., Zhang, P. Z., Molnar, P., Liu, X. W., & Yuan, D. Y. (2013b). Late Quaternary slip rates of the thrust faults in western Hexi Corridor (Northern Qilian Shan, China) and their implications for northeastward growth of the Tibetan Plateau. *Geosphere, 9*(2), 342-354.

Zheng, W., Zhang, P., Yuan, D., Wu, C., Li, Z., Ge, W., Wang, W., & Wang, Y. (2019). Basic characteristics of active tectonics and associated geodynamic process in continental China. *Journal of Geomechanics, 25*(5), 699-721. (in Chinese with English Abstract).

Zhong, Y. (2017). Fluvial Terraces of Tongziba River, Eastern Qilian Shan and Their Responses to Neotectonic Movement and Climate Change. Master's degree thesis of Peking University, Beijing, China, pp. 1-55. (in Chinese with English Abstract).

Zhu, L., & Helmberger, D. V. (1996). Intermediate depth earthquakes beneath the India‐Tibet collision zone. *Geophysical Research Letters*, *23*(5), 435-438.

Zou, X., Yuan, D., Shao, Y., Liu, X., Zhang, B., & Yang, H. (2017). Using stereo-pair and differential GPS to reveal surface deformation characteristics of the Minle-Yongchang fault. *Seismology and Geology. 39*(6), 1198-1212. (in Chinese with English abstract).

Zuza, A. V., Cheng, X., & Yin, A. (2016). Testing models of Tibetan Plateau formation with Cenozoic shortening estimates across the Qilian Shan–Nan Shan thrust belt. *Geosphere*,

581 *12*(2), 501-532.

582

583 **Figure Captions**

584 Figure 1. (a) Topography and active tectonics of the northeast Tibetan Plateau and its peripheral
585 zone with an insert topographic map of the inner Asia in the lower left (Yuan et al., 2013; Zheng
586 et al., 2013b). Boundary fault means fault with unknown kinematics. NQFTS, the north Qilian
587 fold-thrust system. The purple boxes indicate the locations of the two GPS velocity sections in
588 Figure 9. (b) Active tectonics and river system around the Minle Fault. The earthquake data
589 (since the year AD 1917) are downloaded from the website of USGS:
590 http://earthquake.usgs.gov/earthquakes.

591

592 Figure 2. (a) Interpretation of the terraces based on detailed field investigation with a Google
593 image around the Minle Fault as the base map. (b) Photo showing the fault scarps on the
594 Hongshui River terraces faulted by the Minle Fault, with a range shown in Figure 2a. (c) A
595 natural outcrop of the Minle Fault on the terrace T_1 on the west bank of the Hongshui River. T_1 is
596 the youngest terrace faulted by the Minle Fault. F1 and F2 are two branches of the Minle Fault,
597 with thrust angles of 35° ±3° and 27° ±3° , respectively. See the photographing location
598 and angle in Figure 2a.

599

600 Figure 3. Terrace-to-river cross sections in the hanging wall of the Minle Fault, showing the
601 elevations and structures of the terraces. See Figure 2a for the locations of I-I'和 II-II'.

602

603 Figure 4. Sampled sections of the AMS ^{14}C dating samples from the terraces T_5, T_2, and T_1. See
604 Figure 2a for the sampling locations.
605
606 Figure 5. (a) Orthoimage of the Minle Fault in its NW-strike section taken by the UAV. Yellow
607 dots show the camera positions of 230 m above the ground. (b) Interpretation of the terraces
608 based on the high resolution orthoimage. A natural outcrop of the fault was observed on T_1 as
609 shown in Figure 2c. (c) Positions of the control points and check points, with a total number of
610 21 with associated horizontal and vertical errors which control the precision of the DEM. (d)
611 DEM generated from the Orthoimage. Three lines numbered in Arabic numerals across the fault
612 were drawn on each terrace, corresponding with topographic profiles in Figure 6.
613
614 Figure 6. The topographic profiles of the terraces across the Minle Fault. The vertical offset of
615 each terrace is taken from the mean height of the scarps on the three profiles.
616
617 Figure 7. Linear regression analysis of the vertical slip rates of the two terraces through the
618 original point. The fault slip rates in different timescales are determined by the cumulative
619 vertical offsets and abandonment ages of terraces, the data of which are shown in Figure 6 and
620 Table 1, respectively. The gray shaded envelope displays the uncertainty of the regression.
621
622 Figure 8. Slip rate of faults or folds within the Hexi Corridor. The slip rates and corresponding
623 references are shown in the white boxes whose arrows point to the research sites. V, H, and S
624 represent the vertical slip rates, the horizontal slip rates, and shorting rates, respectively. Marks in

625 the same shape represent the results on the same fault, and colors indicate different sites. Each
626 fault or fold is coded with a combination of a letter and a number. The bold lines and fonts
627 represent the NQFTS. F1, Yumen Fault (YMF); F2, Fodongmiao-Hongyazi Fault (FHF); F3,
628 North Yumu Shan Fault (NYSF); F4, East Yumu Shan Fault (EYSF); F5, Minle-Damaying Fault
629 (MDF); F6, Huangcheng-Taerzhuang Fault (HTF); F7, Hanxia-Dahuanggou Fault (HDF); F8,
630 Hei Shan Fault; F9, Jintanan Shan Fault; F10, South Heli Shan Fault (SHSF); F11, South
631 Longshou Shan Fault (SLSF); F12, Minle-Yongchang Blind Fault; F13, Fengle Fault; F14,
632 Kangingqiao Fault; A1, Laojunmiao Antice; A2, Yumu Shan Anticline; A3, Yonggu Anticline;
633 A4, Nanying Anticline.
634
635 Figure 9. GPS observation velocity in the two sections across the Zhangye Basin in the direction
636 of N45°E. The position of the two profiles are shown in Figure 1. The blue dots and error bars
637 refer to the rates of movement recorded by GPS stations relative to the stable Eurasian continent
638 between 2009 and 2017. Six and eleven GPS stations are used in the section (a) and (b),
639 respectively (Table S1; Zheng et al., 2017b). The red and green lines represent faults and folds,
640 respectively. The gray lines show the mean elevation of the 5 km-wide strip of each section from
641 south to north. SQF, Sunan-Qilian Fault; YSA, Yumu Shan Anticline; HYF, Haiyaun Fault; YGA,
642 Yonggu Anticline; NLSF, North Longshou Shan Fault.

643 **Table**

644 Table 1. AMS ^{14}C Dating Data of the Hongshui River Terraces

Sample No.[a]	Sampled Terrace level	Sample location	Terrace elevation of the sampling site (m)[b]	Sampling depth (m)[c]	Conventional ^{14}C age (a BP)	Calibrated ^{14}C cal age (cal a BP)[d]	Terrace abandonment age (cal a BP)
MLF97	T_1	100°49'55.02" E, 38°18'56.50" N	2511	2.7	8590 +/- 30	9560±44	9310±87
MLF123		100°49'29.49"E, 38°21'45.90"N	2430	1.1	8200 +/- 30	9149±117	
MLF125				1.1	8250 +/- 30	9222±100	
MLF79	T_2	100°48'52.76" E, 38°23'40.09" N	2359	1.3	13970 +/- 40	16938±219	17513±185
MLF113		100°50'2.89" E, 38°19'13.93" N	2509	0.9	16920 +/- 50	20396±191	
MLF25		100°50'26.63" E, 38°18'17.36" N	2548	3.3	12760 +/- 40	15205±145	
MLF38	T_5	100°49'0.22" E, 38°23'49.61"N	2374	2.2	38040 +/- 330	42255±465	42255±465
MLF39				3.9	43200 +/- 630	46536±1303	

645 Note: [a] The dating process of AMS ^{14}C was conducted in the Beta Laboratory. See the sampling

646 locations and the sampled sections in Figure 2a and Figure 3, respectively. [b] The longitude

647 and latitude of the samples and the terrace elevation were obtained by a Garmin handheld

648 GPS. [c] The sampling depth was measured by a tape with the scale of 1 cm. [d] IntCal13

649 atmospheric curve (Reimer et al. 2013) were applied in the laboratory for the calibration of

650 the ^{14}C age, with an uncertainty of a 2 σ . Half-life of 5568 years was used for calculation

651 and dates were reported as years before present (present=AD 1950).

652 Table 2. Slip rate of faults and folds in the Hexi corridor

Fault/ Fold	Reference	Total slip rate (mm • a^{-1})	Vertical slip rate (mm • a^{-1})	Shortening rate (mm • a^{-1})	Period (ka)	Dating Method	Thrust Angle	Longitude (° E)	Latitude (° N)
Laojunmiao Anticline (A1)	*Hetzel et al., 2006*	/	0~0.8±0.2	0~2.2±0.5	61±10~10.1±7.1	^{10}Be	/	97.538	39.771
	Liu et al., 2019b	/	/	1.9±0.5	21.6±1.4	^{10}Be	/	97.713	29.702
Yumen Fault (F1)	*Liu et al., 2017*	/	V_a: 0.67±0.08	1.26±0.31	44.9±4.8	^{10}Be	30° ±5°	97.842	39.695
		/	V_b: 0.76±0.09		24.2±2.5				
		/	V_c: 0.71±0.08		17.5±1.9				
		/	V_d: 0.78±0.09		12.6±1.4				
	Li et al., 2016	/	V_a: 0.24~0.30	0.34~1.03	46.9±4.3	^{10}Be	30° ±5° ①	98.021	39.619
		/	V_b: 0.41~0.48		11.05±1.40	OSL			
Fodongmiao-Hongyazi Fault (F2)	*Yang et al., 2018a*	/	V_{1a}: 1.2±0.1	1.0~1.4	206.7±10.5	^{10}Be	40° ±10°	98.416	39.530
		/	V_{1b}: 2.4±0.1		47.4±2.0				
		/	V_{2a}: 1.0±0.2	0.7~1.2	45.8±5.3			98.808	39.367
		/	V_{2b}: 0.8±0.1		22.0±1.4				
		/	V_{2c}: 0.6±0.1		13.8±1.1				
		/	V_{2d}: 0.8±0.1		6~7.3	OSL&^{14}C			
	Liu et al., 2019a	/	V_1: 1.0±0.3	1.4±0.5	16.3±1.3	OSL	40° ±10°	98.522	39.481
		/	V_2: 0.9±0.2	1.2±0.4	9.5~9.7	^{14}C		99.173	39.207
	Yang et al., 2018b	/	/	0.8±0.2	16.7±1.5	^{10}Be	/	99.078	39.252
	Hetzel et al.，2019	/	V_a: 1.22±0.45	S_a: 2.1±0.5	153±12	^{10}Be	30° ±5°	98.404	39.518
		/	V_b: 1.17±0.39	S_b: 2.0±0.4	100±7				
		/	V_c: 0.87±0.29	S_c: 1.5±0.3	58.9±3.7				
		/	V_d: 0.93±0.35	S_d: 1.6±0.4	22.5±2.2				
Yumu Shan Anticline (A2)	*Hu et al., 2019*	/	/	1.25±1.10	92±6	^{10}Be	/	100.013	38.973
North Yumu Shan Fault (F3)	*Chen et al., 2017*	/	V_1: 0.73±0.14	S_1: 0.59±0.26	~15	OSL	43° ~61° ②	99.642	39.250
		/	V_2: 0.27±0.04	S_2: 0.22±0.09	~8	OSL		99.600	39.253

	Palumbo et al., 2009	/	V_{1a}: 0.77±0.10	S_{1a}: 0.63±0.25	35.1±2.3	^{10}Be	43° ~61° ②	99.770	39.219
		/	V_{1b}: 0.48±0.15	S_{1b}: 0.39±0.21	15.5±2.3				
		/	V_2: 0.56±0.06	S_2: 0.46±0.18	113.4±4.9			100.046	39.008
	Hu et al., 2019	/	0.61±0.16	0.47±0.33	92±6	^{10}Be	55° ±15°	100.046	39.008
East Yumu Shan Fault (F4)	*Ren et al., 2019*	/	V_1: 1.1	S_1: 0.29~0.64	38.04±5.04	OSL	60° ~75° ③	100.104	38.901
		/	V_2: 0.3~0.4	S_2: 0.09~0.12	22.4~23.3		73°	100.115	38.833
	Qi , 2017	/	V_a: 1.25	0.33~0.88	47.0±3.4	OSL	60° ~75° ③	100.115	38.833
		/	V_b: 1		19.69±1.32				
	Cao et al., 2019	/	1.0±0.2	0.8±0.1	88.7±7.0	^{10}Be	/	100.230	38.750
Sorth Heli Shan Fault (F10)	*Zheng et al., 2013a*	/	V_1: 0.1~0.14	S_1: 0.1~0.2	~15	OSL	40° ~65°	99.560	39.746
		/	V_2: 0.2~0.3	/	~13			99.834	39.674
		/	V_3: 0.15~0.25	S_3: 0.4~0.5	~18			100.085	39.579
Minle Fault	*This study*	/	V_a: 0.54±0.02	0.95±0.30	42.3±0.5	AMS ^{14}C	31° ±7°	100.824	38.372
		/	V_b: 0.49±0.01		16.9±0.2				
Minle-Damaying Fault (F5)	*Zhong，2017*	/	V_a: 1.05±0.31	1.02±0.6	10.09±0.03	AMS ^{14}C	50° ±10°	100.934	38.212
		/	V_b: 0.62±0.33		8.13±0.07				
		/	V_c: 0.70±0.67		2.90±0.06				
		/	V_d: 7.04±5.04		0.3±0.02				
	Xiong et al., 2017	/	V_a: 0.96±0.11	0.83~1.91	12.7±1.4	OSL	35±5°	101.559	37.843
		/	V_b: 1.10±0.07		5.8±0.1	AMS ^{14}C			
		/	V_c: 1.03±0.04		4.5±0.1				
Yonggu Anticline (A3)	*Zhong，2017*	/	/	S: 1.50±0.06	10.09±0.03	AMS ^{14}C	/	100.938	38.402
Huangcheng-Taerzhuang Fault (F6)	*Chen，2003*	/	V_1: 0.82	S_1: 0.85±0.23	10.0±0.6	SL	39° ~50°	103.020	37.592
		/	V_2: 0.54	S_2: 0.56±0.15	~5			102.543	37.662
		/	V_{3a}: 1.02±0.09	S_3: 0.90±0.35	39.2±3.1			102.773	37.608
		/	V_{3b}: 0.69±0.04		30.6±2.4				

		/	V_{3c}: 0.68±0.05		19.8±1.5				
Nanying Anticline (A4)	*Hu et al., 2015*	T_a: 0.5±0.4	/	0.8±0.2	34±3	OSL	/	102.482	37.796
		T_b: 0.8±0.1			57±4				
		T_c: 0.9±0.2			69±4				
Kangningqiao Fault (F14)	*Ai et al., 2017*	/	V_a: 0.46±0.04	0.48±0.04	7.61±0.05	AMS ^{14}C	45°	102.417	37.964
		/	V_b: 0.50±0.03		6.40±0.09				

Note: T, V, S means total slip rate, vertical slip rate, and shortening rate, respectively. The blue words are rates calculated by ourselves. Number subscripts (e.g. V_1, S_2) represent slip rate of the fault/fold at different places, while letter subscripts (e.g. V_a, S_b) represent slip rate during different periods. ①② ③refer to Liu et al., 2017, IGLS,1993 and Li et al., 1997, respectively.

Figure 1.

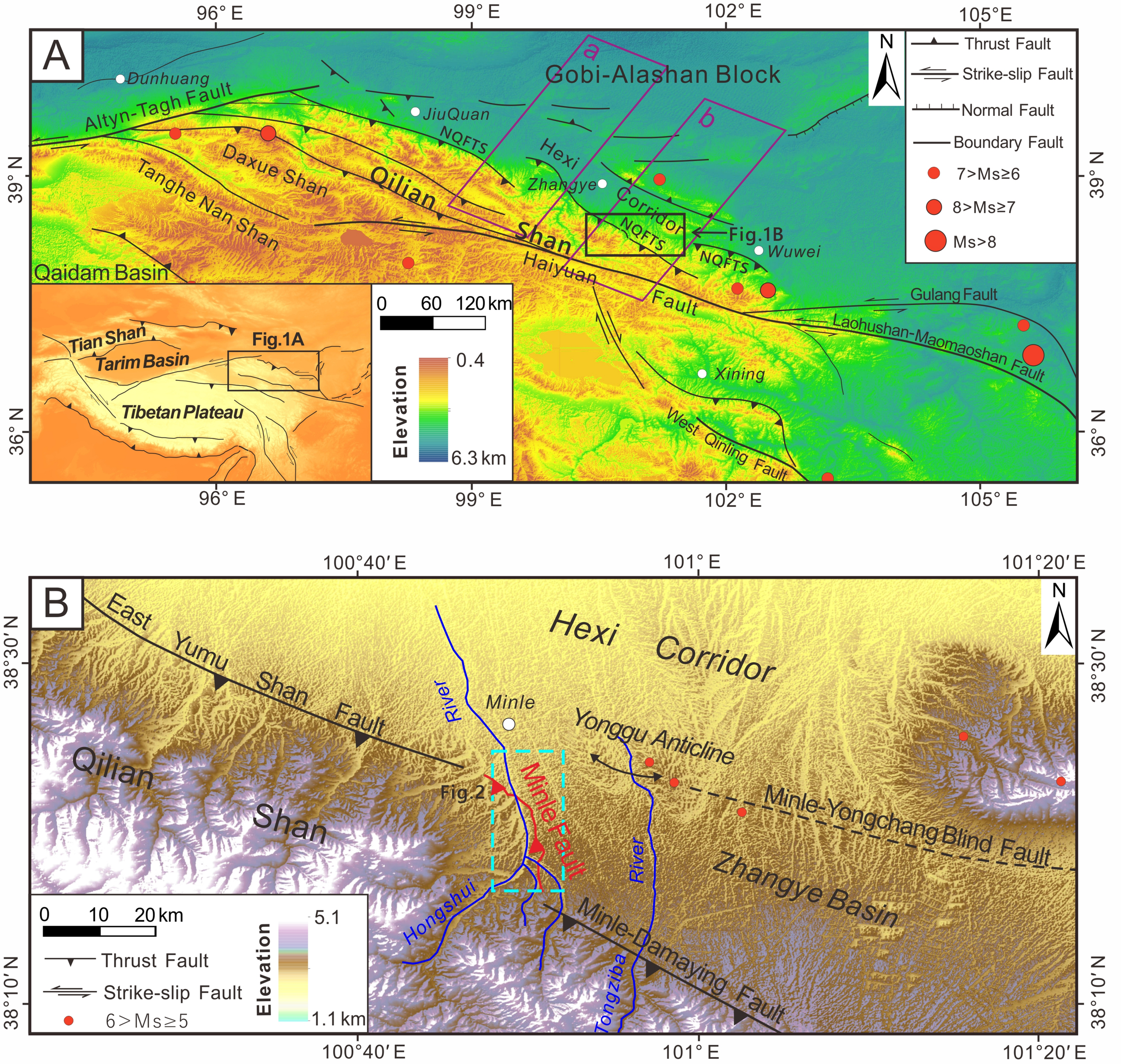
A
96° E
99° E
102° E
105°E
39° N
36° N
Dunhuang
Altyn-Tagh Fault
JiuQuan
NQFTS
Daxue Shan
Tanghe Nan Shan
Qilian Shan
Qaidam Basin
a
b
Gobi-Alashan Block
Hexi Corridor
Zhangye
Fig.1B
Wuwei
Haiyuan Fault
Gulang Fault
Laohushan-Maomaoshan Fault
Xining
West Qinling Fault
N
Thrust Fault
Strike-slip Fault
Normal Fault
Boundary Fault
7>Ms≥6
8>Ms≥7
Ms>8
Tian Shan
Tarim Basin
Fig.1A
Tibetan Plateau
0 60 120 km
Elevation
0.4
6.3 km
B
100°40′ E
101° E
101°20′ E
38°30′ N
38°10′ N
East Yumu Shan Fault
Qilian Shan
Hexi Corridor
River
Minle
Fig.2
Minle Fault
Yonggu Anticline
Minle-Yongchang Blind Fault
Hongshui
Zhangye Basin
Minle-Damaying Fault
Tongziba
0 10 20 km
Thrust Fault
Strike-slip Fault
6>Ms≥5
Elevation
5.1
1.1 km

Figure 2.

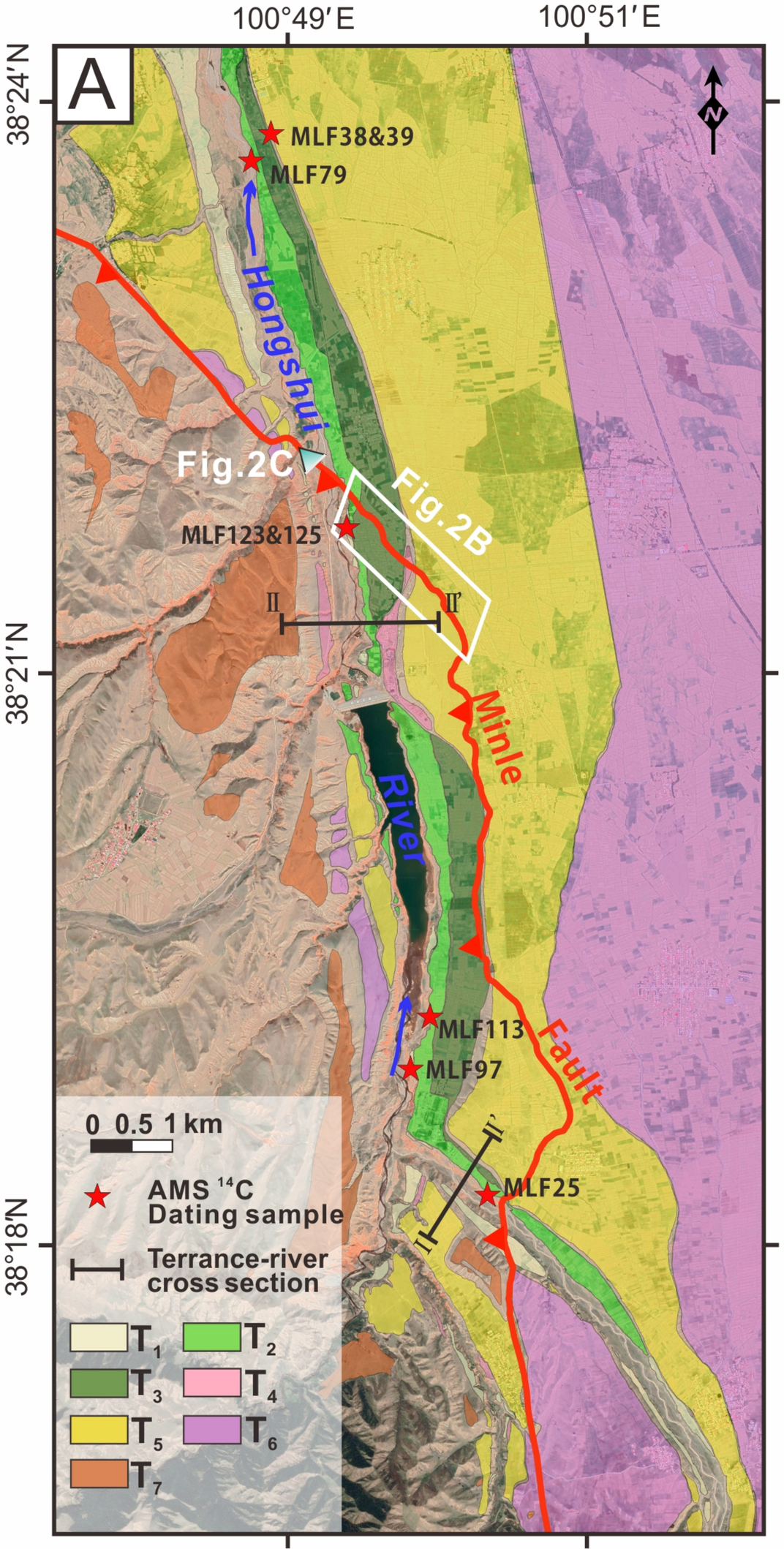
A
100°49′E
100°51′E
38°24′N
38°21′N
38°18′N
MLF38&39
MLF79
Hongshui
Fig.2C
Fig.2B
MLF123&125
Ⅱ
Ⅱ′
Minle
River
MLF113
MLF97
Fault
Ⅱ′
MLF25
0 0.5 1 km
AMS 14C Dating sample
Terrance-river cross section
T1
T2
T3
T4
T5
T6
T7

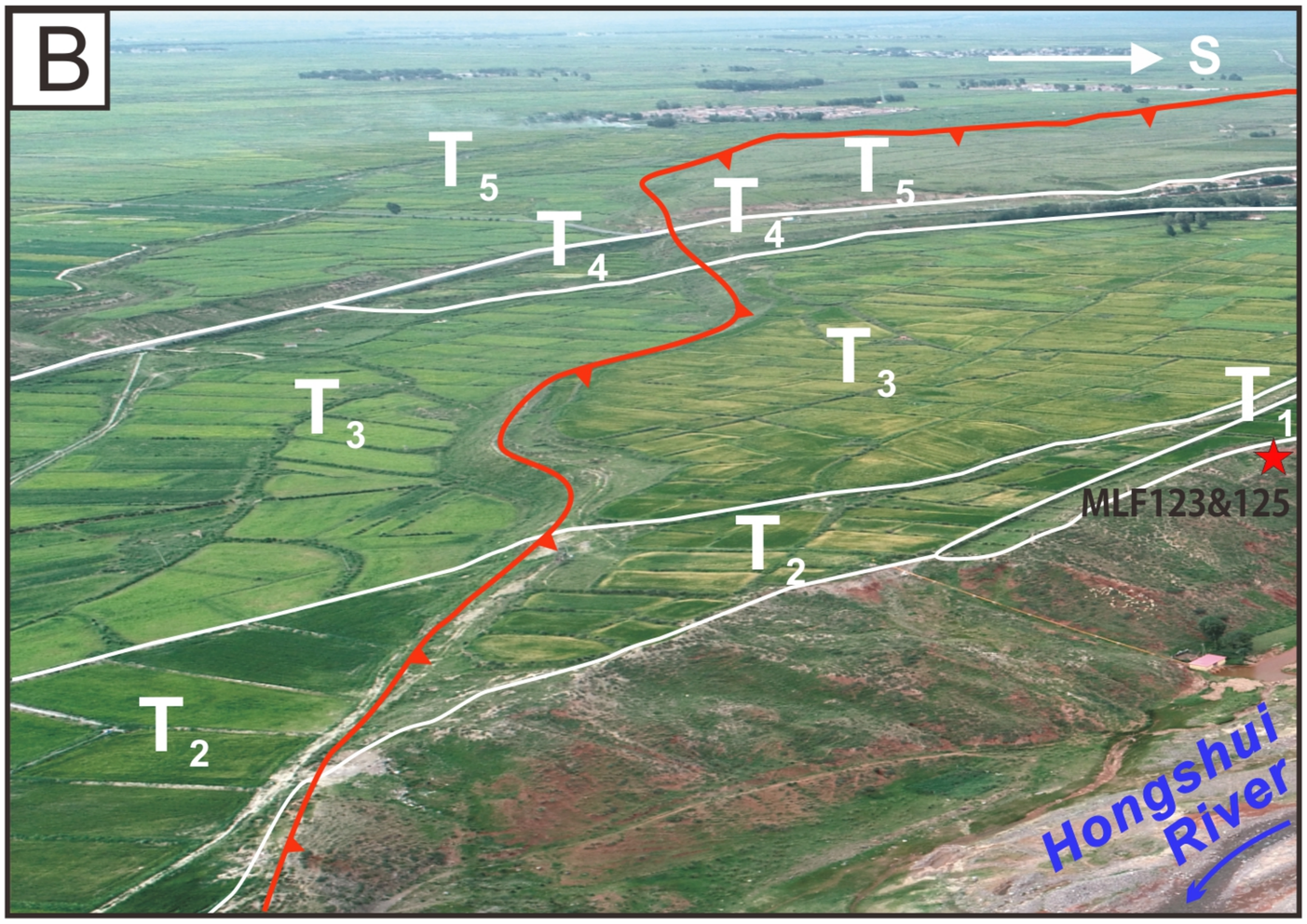
B
S
T5
T4
T4
T5
T3
T3
T1
MLF123&125
T2
T2
Hongshui River

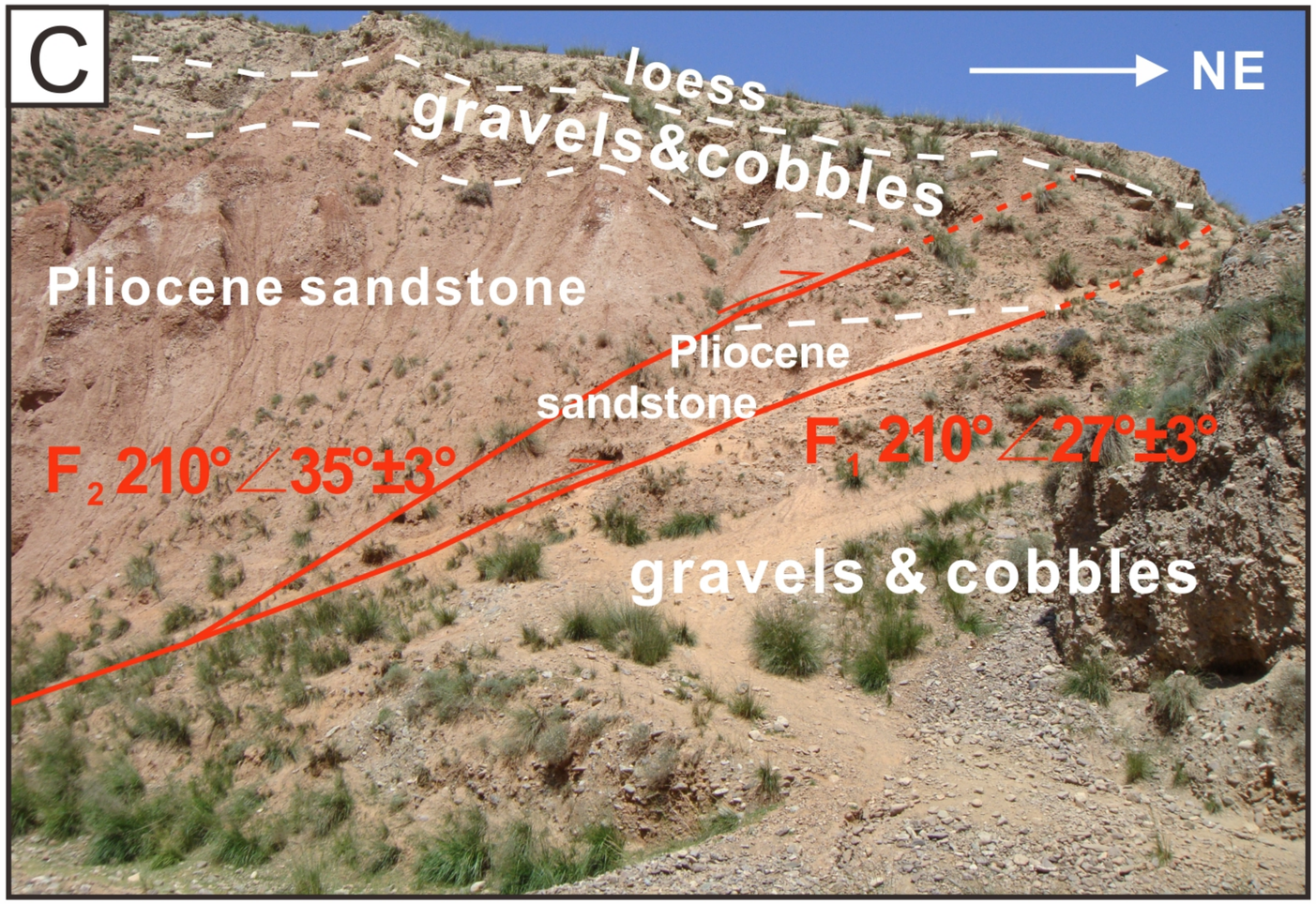
C
NE
loess
gravels&cobbles
Pliocene sandstone
Pliocene sandstone
F2 210°∠35°±3°
F1 210°∠27°±3°
gravels & cobbles

Figure 3.

Elevation (m)

2550
2500
2450
2400
2350

II
T_7
T_4
T_2
T_3
T_4
T_5
II'

loess sediment
gravels& cobbles
Pliocene sandstone

Hongshui River

2550
2525
2500
2475

I
T_5
T_1
T_2
T_3
T_5
I'

Yudai River

0
500 m

Figure 4.

Terrace T_1

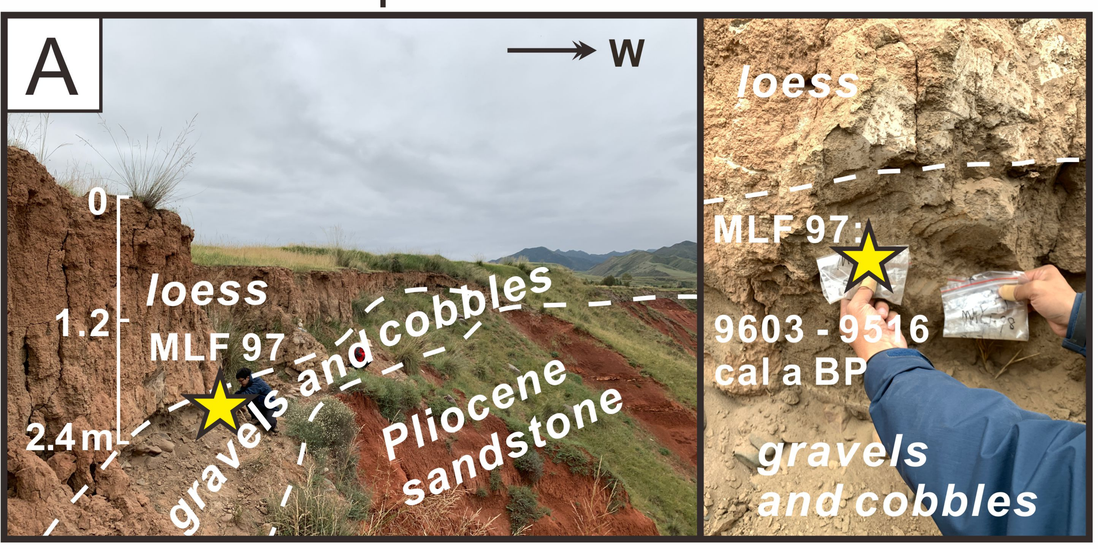

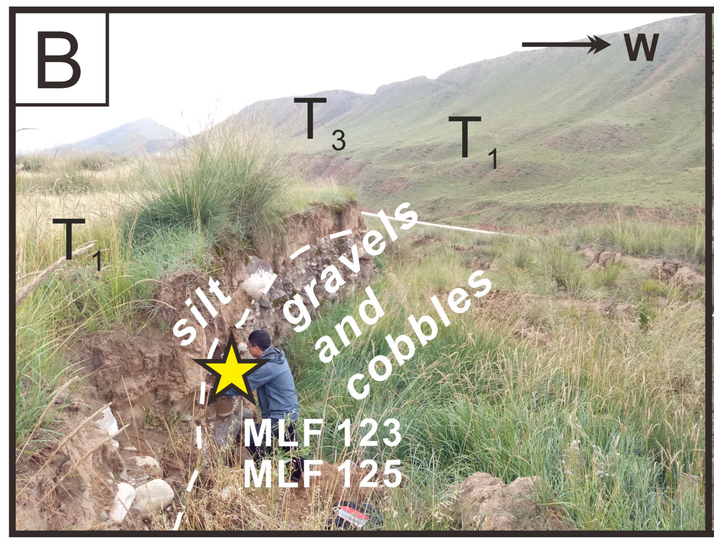

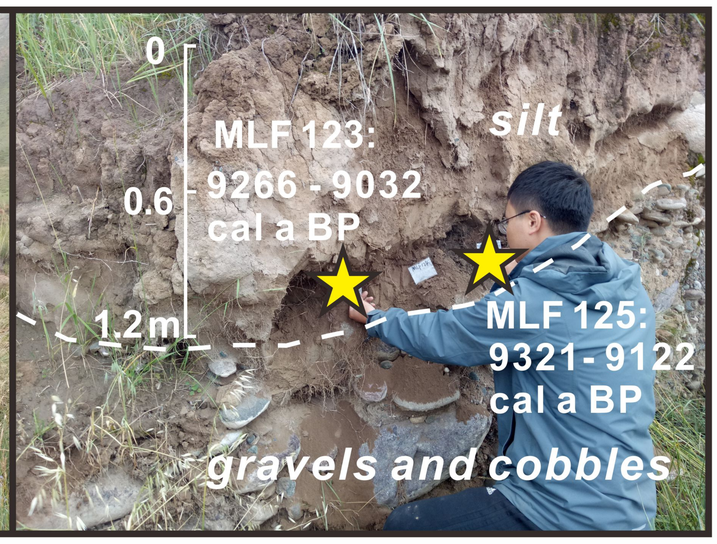

Terrace T_2

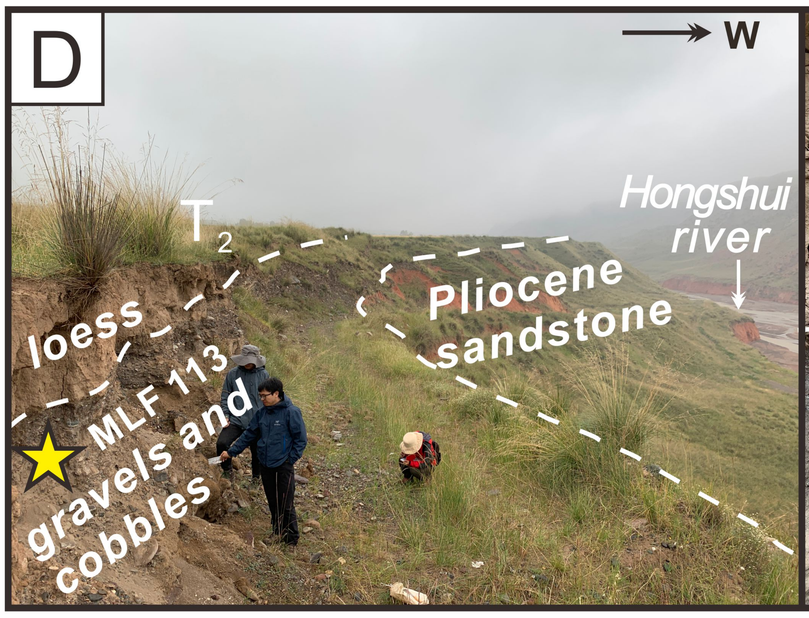

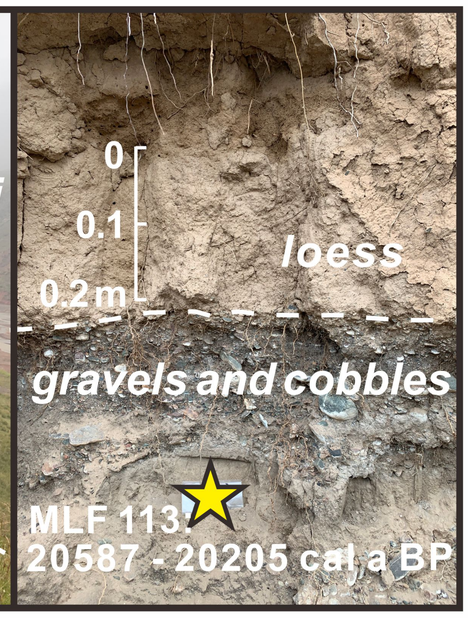

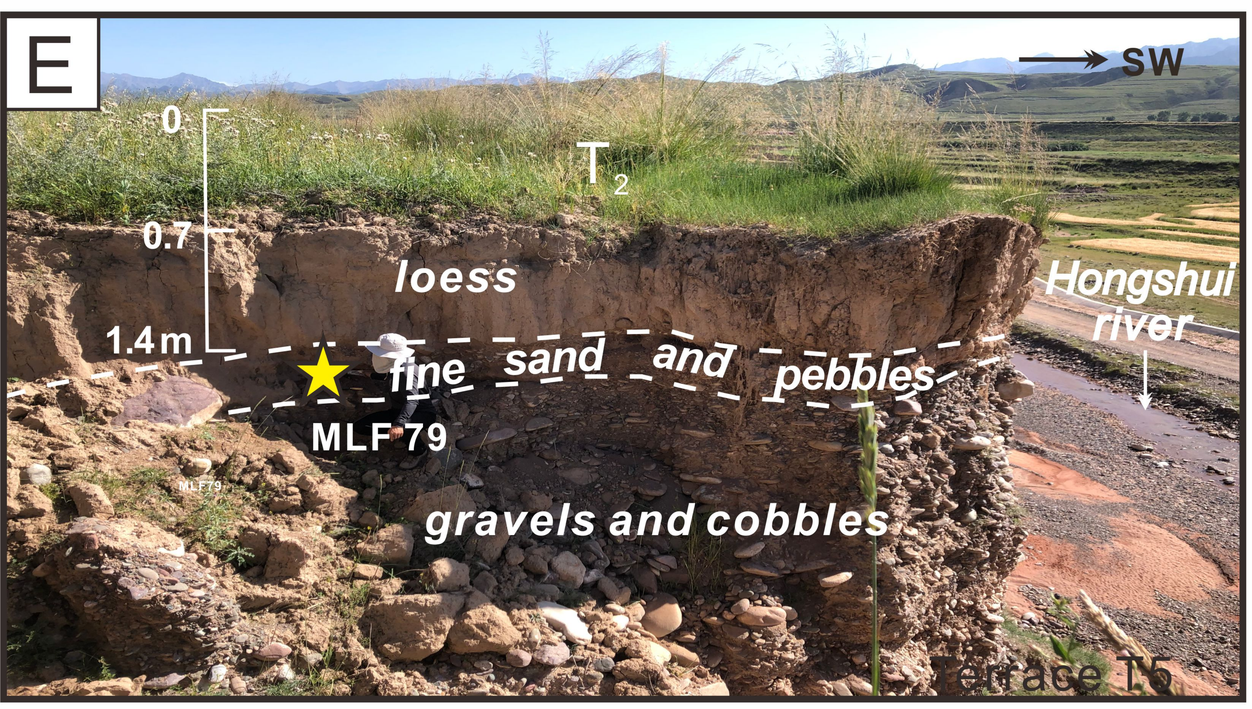

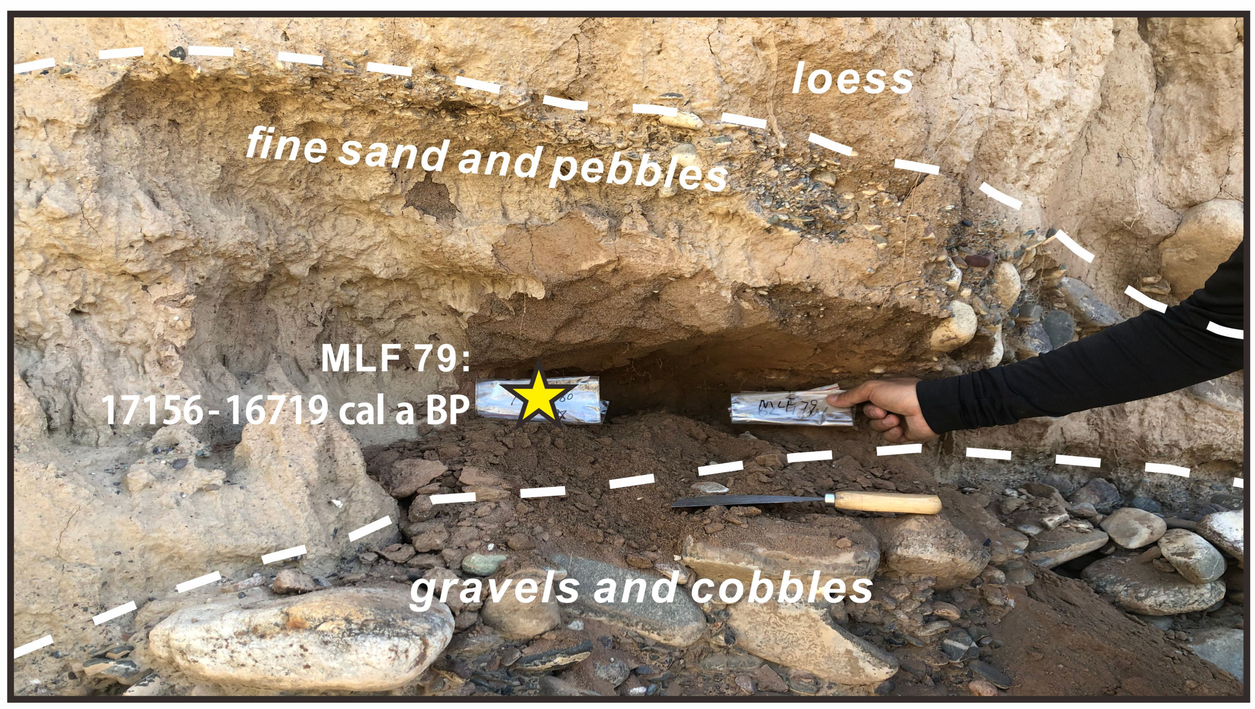

Terrace T_5

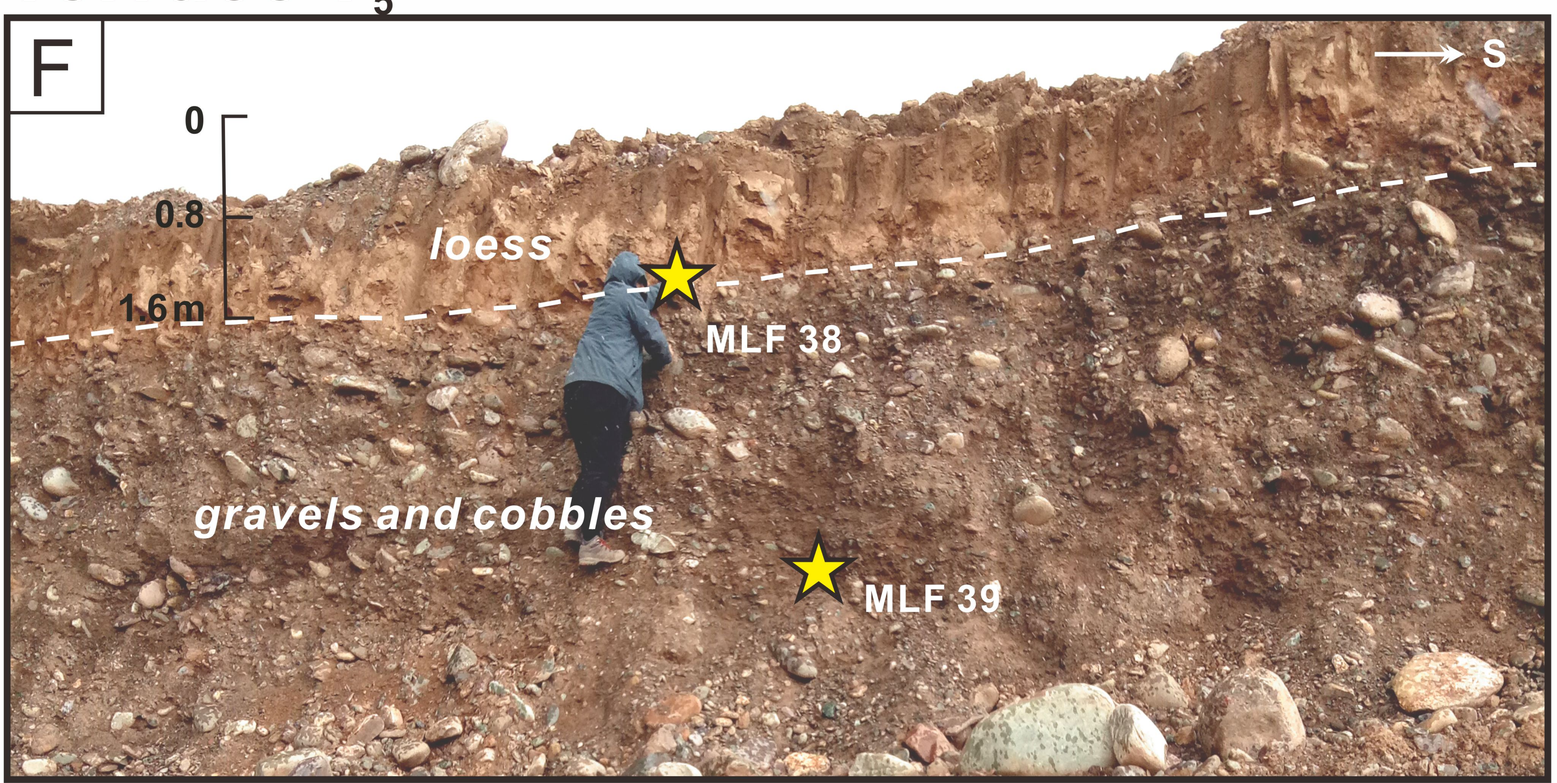

Figure 5.

A

N

0 250 500 m

Hongshui River

Minle Fault

camera position

B

N

0 250 500 m

T_1 T_2 T_3 T_4 T_5

Hongshui River

Minle Fault

C

N

0 250 500 m

control point

check point

Horizontal error:

5 cm

Vertical error:

50~90 cm

20~50 cm

0~20 cm

-30~0 cm

-60~-30 cm

-74.63 cm

Hongshui River

Minle Fault

D

N

0 250 500 m

Elevation

2447.1

2332.2 m

T_2 T_3 T_4 T_5

Hongshui River

Minle Fault

Figure 6.

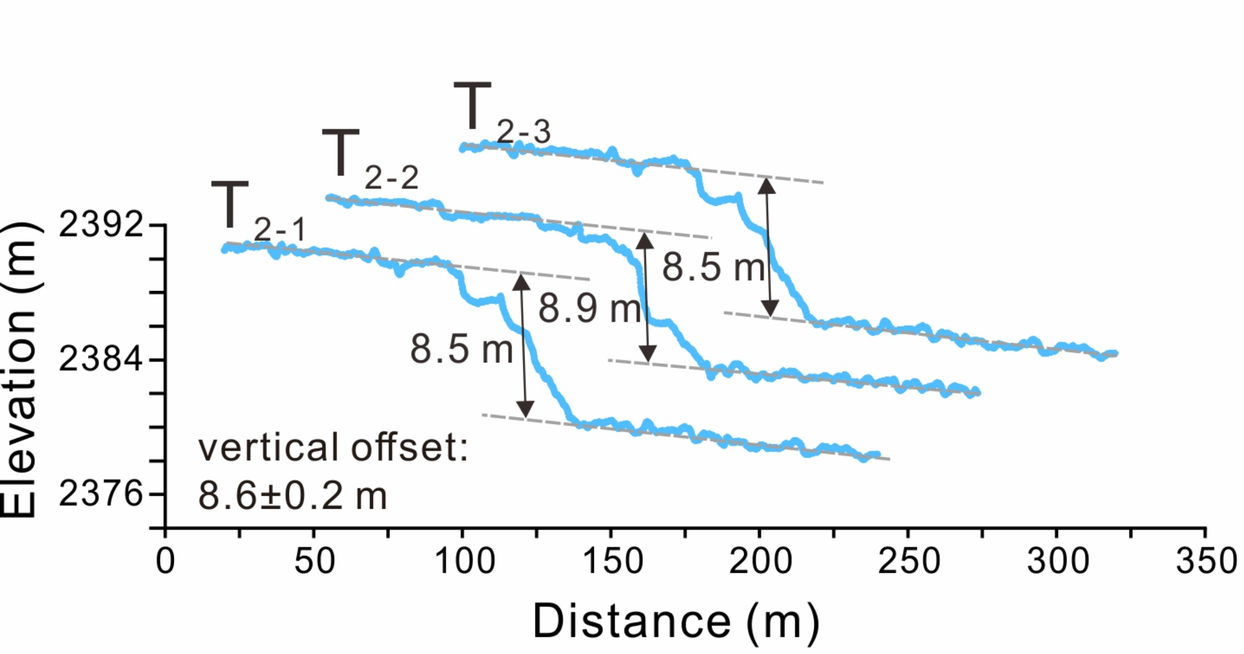
T2-1
T2-2
T2-3
8.5 m
8.9 m
8.5 m
vertical offset:
8.6±0.2 m
Elevation (m)
2392
2384
2376
0
50
100
150
200
250
300
350
Distance (m)

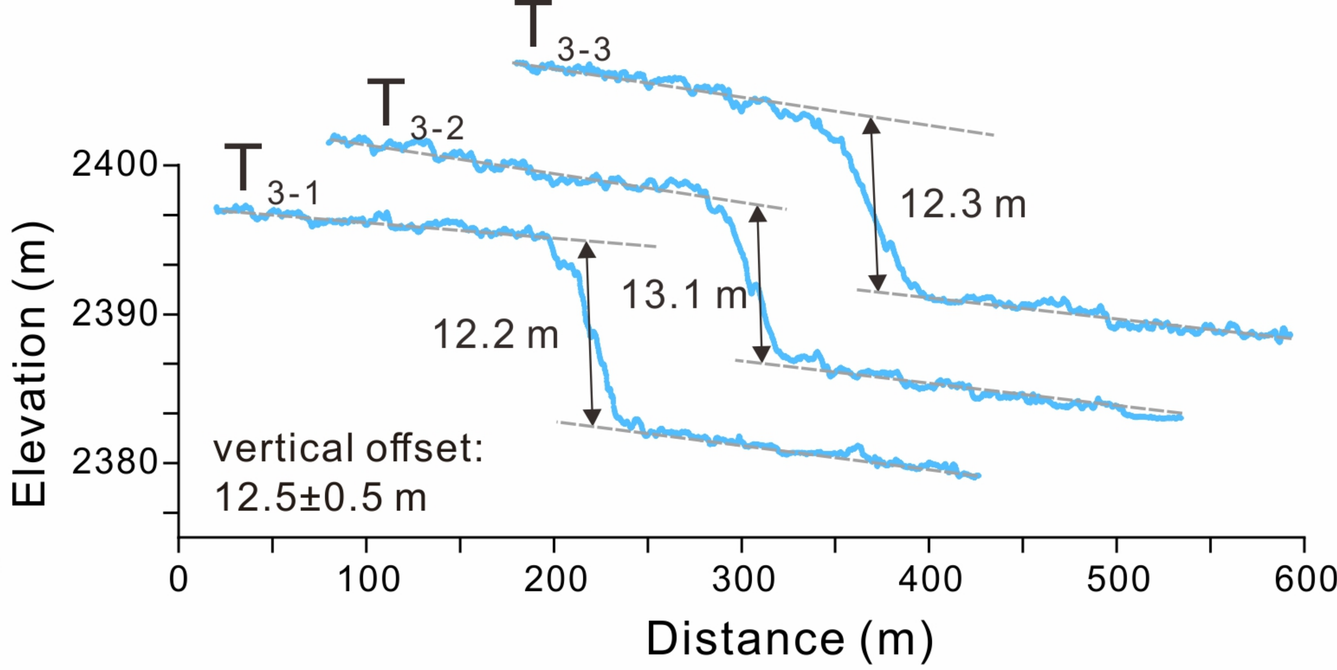
T3-1
T3-2
T3-3
12.2 m
13.1 m
12.3 m
vertical offset:
12.5±0.5 m
Elevation (m)
2400
2390
2380
0
100
200
300
400
500
600
Distance (m)

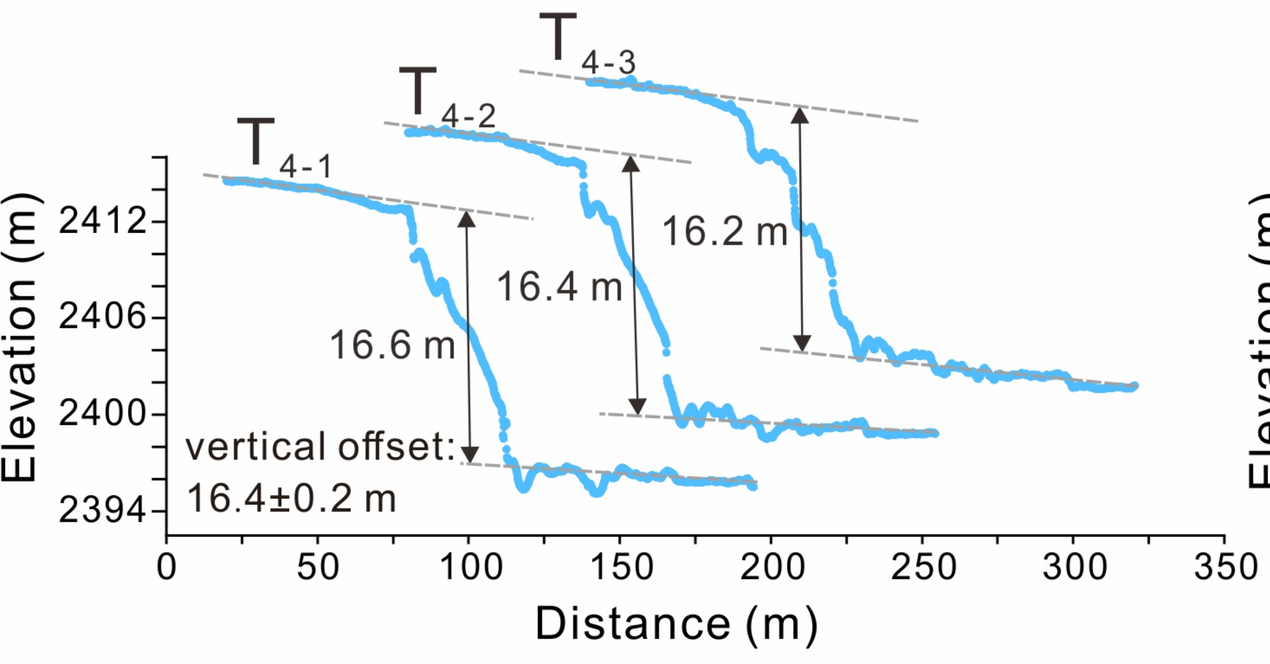
T4-1
T4-2
T4-3
16.6 m
16.4 m
16.2 m
vertical offset:
16.4±0.2 m
Elevation (m)
2412
2406
2400
2394
0
50
100
150
200
250
300
350
Distance (m)

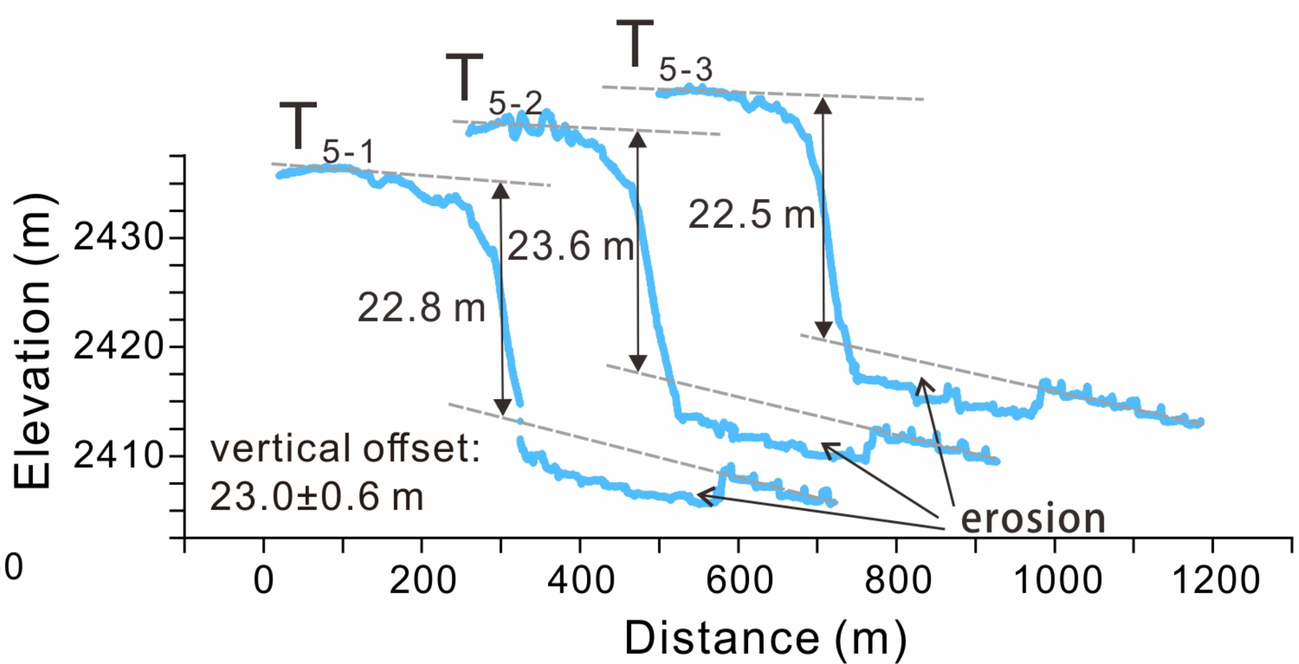
T5-1
T5-2
T5-3
22.8 m
23.6 m
22.5 m
vertical offset:
23.0±0.6 m
erosion
Elevation (m)
2430
2420
2410
0
200
400
600
800
1000
1200
Distance (m)

Figure 7.

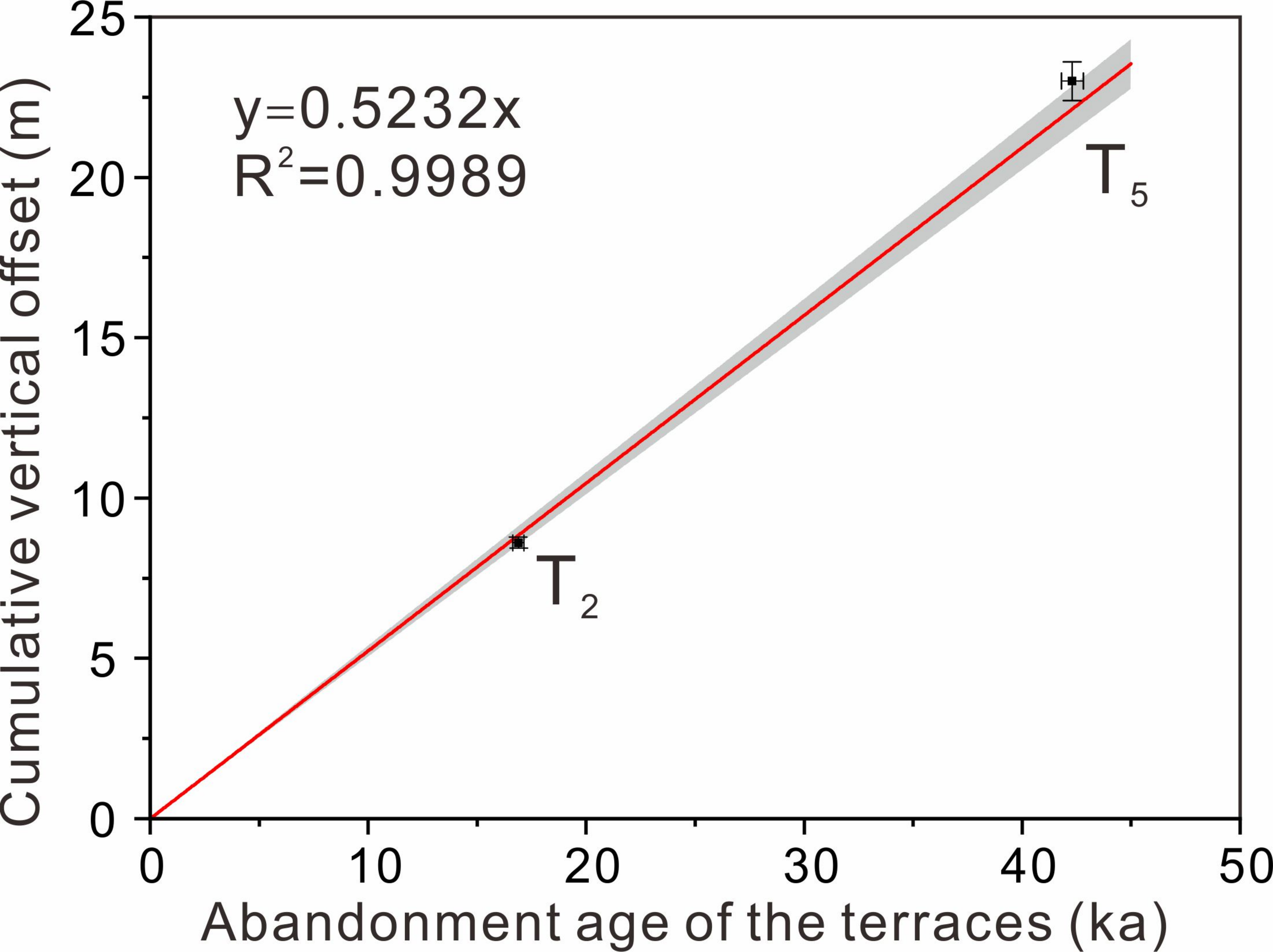
y=0.5232x
R²=0.9989
T5
T2
Cumulative vertical offset (m)
Abandonment age of the terraces (ka)
0
5
10
15
20
25
0
10
20
30
40
50

Figure 8.

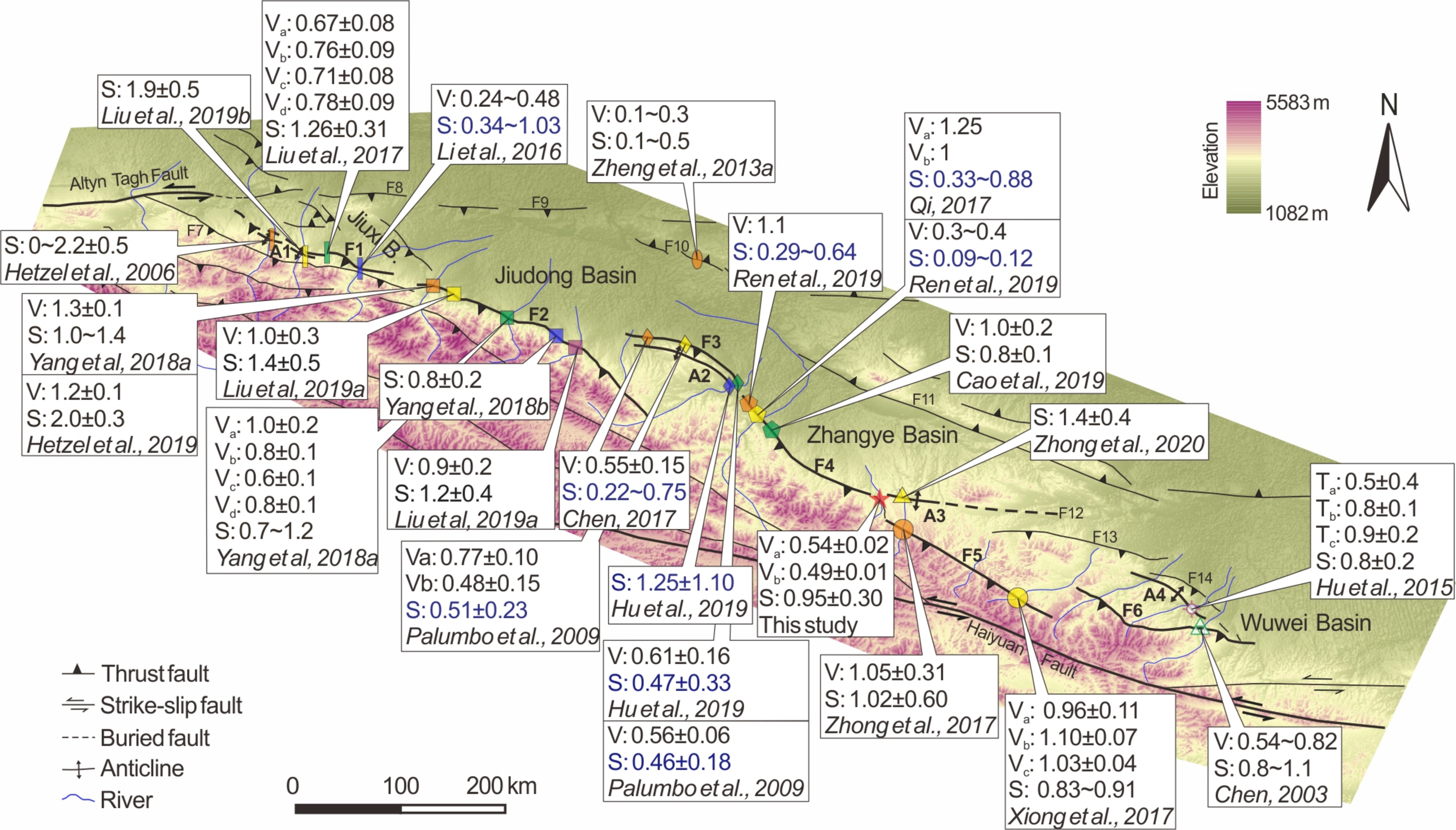
S: 1.9±0.5
Liu et al., 2019b
Va: 0.67±0.08
Vb: 0.76±0.09
Vc: 0.71±0.08
Vd: 0.78±0.09
S: 1.26±0.31
Liu et al., 2017
V: 0.24~0.48
S: 0.34~1.03
Li et al., 2016
V: 0.1~0.3
S: 0.1~0.5
Zheng et al., 2013a
Va: 1.25
Vb: 1
S: 0.33~0.88
Qi, 2017
V: 0.3~0.4
S: 0.09~0.12
Ren et al., 2019
V: 1.1
S: 0.29~0.64
Ren et al., 2019
S: 0~2.2±0.5
Hetzel et al., 2006
V: 1.3±0.1
S: 1.0~1.4
Yang et al, 2018a
V: 1.2±0.1
S: 2.0±0.3
Hetzel et al., 2019
V: 1.0±0.3
S: 1.4±0.5
Liu et al, 2019a
S: 0.8±0.2
Yang et al., 2018b
V: 1.0±0.2
S: 0.8±0.1
Cao et al., 2019
S: 1.4±0.4
Zhong et al., 2020
Va: 1.0±0.2
Vb: 0.8±0.1
Vc: 0.6±0.1
Vd: 0.8±0.1
S: 0.7~1.2
Yang et al, 2018a
V: 0.9±0.2
S: 1.2±0.4
Liu et al, 2019a
V: 0.55±0.15
S: 0.22~0.75
Chen, 2017
Va: 0.77±0.10
Vb: 0.48±0.15
S: 0.51±0.23
Palumbo et al., 2009
S: 1.25±1.10
Hu et al., 2019
Va: 0.54±0.02
Vb: 0.49±0.01
S: 0.95±0.30
This study
Ta: 0.5±0.4
Tb: 0.8±0.1
Tc: 0.9±0.2
S: 0.8±0.2
Hu et al., 2015
V: 0.61±0.16
S: 0.47±0.33
Hu et al., 2019
V: 0.56±0.06
S: 0.46±0.18
Palumbo et al., 2009
V: 1.05±0.31
S: 1.02±0.60
Zhong et al., 2017
Va: 0.96±0.11
Vb: 1.10±0.07
Vc: 1.03±0.04
S: 0.83~0.91
Xiong et al., 2017
V: 0.54~0.82
S: 0.8~1.1
Chen, 2003
Altyn Tagh Fault
Jiuxi B.
Jiudong Basin
Zhangye Basin
Wuwei Basin
Haiyuan Fault
F1
F2
F3
F4
F5
F6
F7
F8
F9
F10
F11
F12
F13
F14
A1
A2
A3
A4
Elevation
5583 m
1082 m
N
Thrust fault
Strike-slip fault
Buried fault
Anticline
River
0
100
200 km

Figure 9.

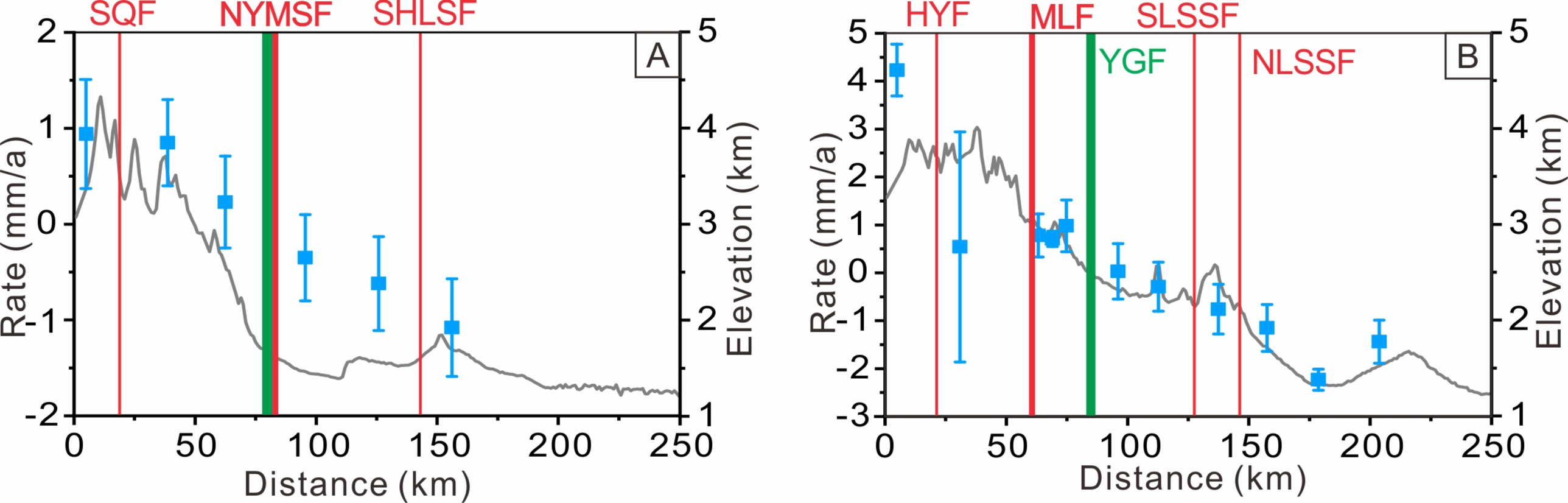
SQF
NYMSF
SHLSF
A
Rate (mm/a)
Elevation (km)
Distance (km)
HYF
MLF
SLSSF
YGF
NLSSF
B
Rate (mm/a)
Elevation (km)
Distance (km)